ANALYSIS OF THE REACTION OF CARBON WITH O_2 USING AB INITIO MOLECULAR ORBITAL THEORY

Takashi Kyotani, and Akira Tomita
Institute for Chemical Reaction Science, Tohoku University,
2-1-1 Katahira, Sendai 980-8577 JAPAN.

KEYWORDS: Carbon gasification, O_2 chemisorption, Ab initio MO theory

INTRODUCTION

The mechanism of carbon gasification with oxygen has been widely studied. It is generally accepted that oxygen molecules chemisorb on carbon free sites to form surface oxygen complexes, C(O), which then desorb as CO_2 and/or CO. We attempted to clarify the mechanism of such reaction processes on carbon surface with several experimental techniques such as temperature programmed reaction and step response experiments using isotopically labeled reactants [1, 2]. In addition to these experimental approaches, molecular orbital (MO) theory is very helpful for the understanding of reaction mechanism. The usefulness of MO theory in the analysis of catalyzed and uncatalyzed carbon gasification has been demonstrated by many researchers [3-10]. Recently, using ab initio MO theory Yang *et al.* theoretically investigated desorption behavior of semiquinone, carbonyl and epoxy oxygen as surface oxygen complexes and discussed the mechanism of carbon gasification with oxygen-containing gases [11]. Furthermore, we have found that it is possible to simulate several experimental results of carbon-NO reaction when ab initio MO theory is applied [12]. Here, we attempted to analyze and simulate the chemisorption process of oxygen molecule and the formation of surface oxygen complexes on carbon edge sites using ab initio MO theory.

CALCULATION METHOD

Both the Gaussian 94 [13] and Gaussian 98 [14] packages were used to calculate molecular orbitals of model compounds for carbon-O_2 system. For simplicity, two types of single layer polyaromatic compounds with different sizes were employed as models for carbon. Figure 1 illustrates the structure of the two types of carbon models (models **A** and **B**) which have zigzag edge site on the upper side of each model. Some of carbon atoms are numbered for convenience. The edge atoms on the upper side are unsaturated and the rest of them are terminated with hydrogen atoms. A single O_2 molecule was put at a given distance from the zigzag edge in two different ways as shown in Figure 2. For side-on mode, the O_2 bond axis is parallel to the edge line. In the case of vertical mode, the bond axis was perpendicular to the plane of carbon model layer.

In order to investigate how O_2 molecule approaches the zigzag edge site of model **A**, we attempted to determine potential energy surface for each of the two approach modes (side-on and vertical). For such calculation, a grid for the position of the O_2 molecule was constructed near the edge site as shown in Figure 3, where each grid point was set in Y direction varying from 0.10 to 0.19 nm with an increment of 0.01 nm and in X direction from the right-hand C(1) atom to the most left-hand one with an increment of 0.01 nm. Thus, the shape of the mesh became square. The center of a single O_2 molecule was put on one of the points and then the following Energy calculation was done. First, the whole system including model **A** and the O_2 molecule was subjected to **UHF** (unrestricted Hartree-Fock) calculation with the basis set of 3-21G(d) with only O_2 bond distance optimized. Then, density functional method using the B3LYP functional with the basis set of 6-31G(d) was applied for single point energy calculation of the whole system with the optimized O-O distance. This energy calculation was done for all the grid points in Figure 3. For each grid point, the heat of adsorption, ΔH, was determined as a difference between the total energy of the calculated system and the sum of the energies of the corresponding carbon model and O_2 molecule. Since only O_2 bond distance was optimized in this grid calculation, the values of ΔH obtained are always a little larger than these determined by a full optimization calculation.

RESULTS AND DISCUSSION

From the grid calculation mentioned above, potential energy surface of O_2 on carbon zigzag site was determined for both side-on and vertical modes. The resultant surface is shown as two contour plots in Figure 4. The abscissa and the ordinate of each plot were defined as the distance in X direction from the right-hand C(1) atom in model **A** and the distance in Y direction from C(1) atoms, respectively. The coordinates in the horizontal axis correspond to geometrical position of the model drawn just below each contour plot. Since the potential energy surface was plotted in terms of ΔH, the thermal stability of the whole system can be evaluated from this value, i.e., the larger value the ΔH, the more unstable the system. For the potential energy surface in side-on mode, there are two minima located at the abscissas of 0.13 and 0.37 nm and at the ordinate of 0.14 nm. These two abscissas correspond to the positions of the two C(2) carbon atoms. This finding suggests that the center of O_2 molecule which is approaching model **A** goes toward either of the two C(2) atoms. Then, the O_2 molecule reaches the minimum at the ordinate of 0.14 nm to form surface oxygen species (model **a**) as illustrated in Figure 5, where O atoms are chemically bound to the C(1) atoms to form a five-membered ring. On the other hand, the result of the vertical approach was quite different from the side-on case. Since the observed three energy minima (Figure 4) are located at the abscissas corresponding to the positions of the C(1) atoms, the center of O_2 molecule is expected to go toward the C(1) atoms. As the result of such approaching, another surface oxygen species (model **b**) as shown in Figure 5 is formed at the ordinate of 0.12 nm. The species consists of a three-membered ring and from the energy contour map it can be seen that its thermal stability is lower than that of model **a**. In both the approach modes, the value of ΔH of each minimum in the contour plots is negative, indicating that the chemisorption of O_2 molecule is an exothermic process. This finding accords with the commonly observed feature for O_2 chemisorption on fresh carbon surface.

We put a single O_2 molecule at a distance of 0.13 nm from the zigzag site of model **B** in either side-on or vertical mode. Then the whole system including model **B** and O_2 was subjected to the ab initio calculation with all the geometrical parameters optimized. As a result, oxygen-containing species similar to model **a** is formed in the case of side-on mode and vertical approach gave model **b**-like structure. The heat of formation, ΔH, for each fully optimized structure was determined. For side-on and vertical approaches, the values were found to be –490 and –270 kJ/mol, respectively, which are not far from the observed one (-410 kJ/mol).

The process simulated in Figure 4 can be regarded as chemisorption of O_2 on fresh carbon surface without any pre-chemisorbed species. It would be worth elucidating the effect of pre-chemisorbed species on the O_2 chemisorption process. For this purpose, we investigated how the presence of either O or H atom on carbon surface influences the structure and the ΔH of the chemisorbed species on zigzag edge site. As a basic model of the edge site, we employed model **B** and bound one or two O atoms to the C(1) atoms as a quinone group. In the case of H atom, we terminated one or two zigzag edge carbon atoms by H atom. After the optimization calculation of these pre-chemisorbed models, we put a single O_2 molecule in the side-on mode on the edge sites. The final optimized structures are illustrated in Figure 6. In every case, a five-membered ring spices similar to model **a** is formed upon the O_2 chemisorption. The values of ΔH are tabulated in Table 1, indicating that there is no noticeable change in ΔH, although the presence of a single C(O) increases the ΔH to some extent.

CONCLUSIONS

Potential energy surface of a single O_2 molecule on carbon zigzag site was determined by the ab initio MO calculation. It was concluded from such calculation that the way of how O_2 molecule approaches the zigzag site depends on the relative position of O_2 to the zigzag site, i.e., side-on or vertical mode. Furthermore, the MO theory predicts that the thermal stability of the O_2-chemisorbed species formed in the side-on mode is higher than that of the vertical case. It was found that the presence of pre-chemisorbed species such as

C(O) or C(H) on zigzag edge site does not influence the structure and the ΔH of O_2-chemisorbed species.

REFERENCES

[1] Zhuang, Q-L.; Kyotani, T.; Tomita, A. *Energy Fuels*, **1995**, 9, 630.
[2] Zhuang, Q-L.; Kyotani, T.; Tomita, A. *Energy Fuels*, **1996**, 10, 169.
[3] Pan, Z. J.; Yang, R. T. *J. Catal.* **1990**, 123, 206.
[4] Chen, S. G.; Yang, R. T. *J. Catal.* **1993**, 141, 102.
[5] Chen, S. G.; Yang, R. T.; Kapteijn, F.; Moulijn, J. A. *Ind. Eng. Chem. Res.* **1993**, 32, 2835.
[6] Janiak, C.; Hoffmann, R.; Sjövall, P.; Kasemo, B. *Langmuir*, **1993**, 9, 3427.
[7] Kyotani, T.; Ito, K.; Tomita, A.; Radovic, L. R. *AIChE J.* **1996**, 42, 2303.
[8] Kyotani, T.; Ogasawara, S.; Radovic, L. R.; Tomita, A. *Proc. Carbon'96*, Newcastle upon Tyne, 1996, 276.
[9] Skokova, K.; Radovic, L. R. *Prepr.-Am. Chem. Soc. Div. Fuel. Chem.* **1996**, 41, 143.
[10] Chen, S. G.; Yang, R. T. *Energy Fuels* **1997**, *11*, 421.
[11] Chen, N.; Yang, R. T. *J. Phys. Chem. A*, **1998**, 102, 6348.
[12] Kyotani, T.; Tomita, A. *J. Phys. Chem. B*, **1999**, 103, 3434.
[13] Frisch M. J. et al. Gaussian 94, Revision E.2, Gaussian, Inc., Pittsburgh PA, 1995.
[14] Frisch M. J. et al. Gaussian 98, Revision A.7, Gaussian, Inc., Pittsburgh PA, 1998.

Table 1 Heat of adsorption of O_2-chemisorbed species. (ΔH for model **B** without any pre-chemisorbed species is –490 kJ/mol.)

Structure	ΔH (kJ/mol)
c	-550
d	-500
e	-480
f	-480

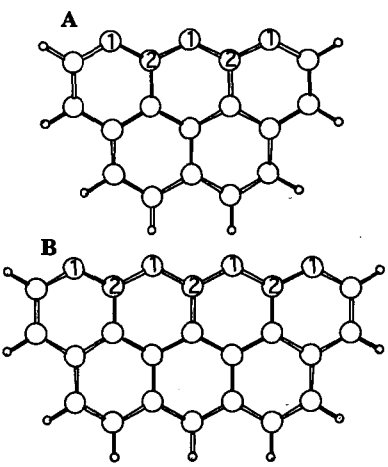

Fig. 1 Selected models of carbon. Large and small circles stand for carbon and hydrogen atoms, respectively.

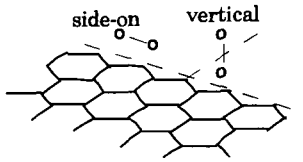

Fig. 2 Two positions of O_2 molecule near carbon edge site

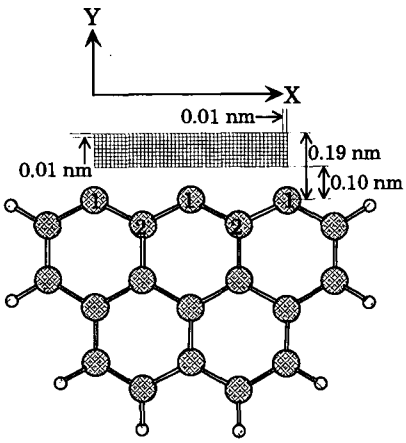

Fig. 3 Grid points for the energy calculation of the system of model **A** and O_2 molecule.

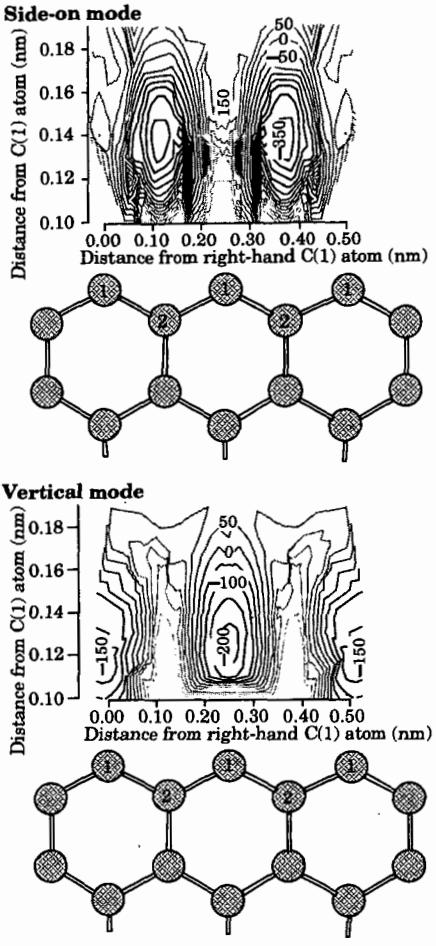

Fig. 4 Energy potential contour map for the carbon-O_2 system. Each contour line corresponds to a heat of reaction for this system and each line is drawn by the step of 50 kJ/mol.

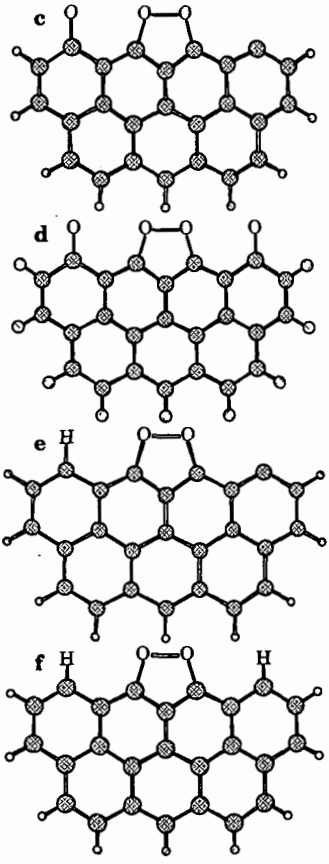

Fig. 6 Surface oxygen complexes formed by O_2 chemisorption on the *zigzag site* in *side-on mode*.

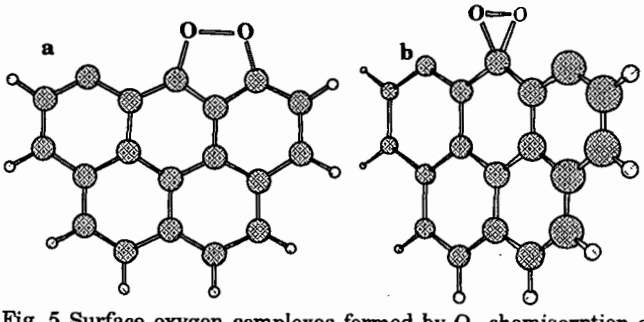

Fig. 5 Surface oxygen complexes formed by O_2 chemisorption on the zigzag site of model **A** in side-on and vertical modes.

ELECTRON DENSITY IN GRAPHENE LAYERS: IMPLICATIONS FOR CARBON REACTIVITY

Ljubisa R. Radovic and Kristina A. Skokova*
Department of Energy and Geo-Environmental Engineering
The Pennsylvania State University, University Park, PA 16802
**BP Amoco Polymers, Alpharetta, GA*

KEYWORDS: Molecular modeling, gasification, carbon reactivity

INTRODUCTION

Much has been accomplished in the last few decades to eliminate empiricism from the kinetic treatments of the combustion and gasification of coals, carbons and graphite (1). However, our ability to further quantify the important details of carbon reactivity is now at a critical juncture from both the experimental and the theoretical point of view. The experimental determination of active and reactive surface areas -- typically straightforward but sometimes tedious and complicated by stringent accuracy requirements -- does lead to satisfactory predictions of reactivity as a function of both carbon nature and carbon burnoff. Although not many such results are available in the literature, they do lend support to recent predictions (2,3) that the turnover frequency at the free carbon sites may be burnoff-dependent. In other words, it is not sufficient to know the carbon's total, active and reactive surface areas to understand all the important details of its reactivity behavior; the rate constant normalized with respect to the reactive area may be burnoff-dependent because the dynamics of surface coverage affect not only the number of sites but also their reactivity (3). In such circumstances, experimental complications increase further and mapping the intrinsic reactivity against the important variables (heat-treatment temperature, reaction temperature, pressure, extent of burnoff) remains quite a challenge.

On the other hand, while the *ab initio* molecular modeling of chemical reactions (4) has become possible and is now widely practiced, the extrapolation from either graphite or polyaromatic hydrocarbons to the carbons of interest (e.g., coal chars) is still subject to much uncertainty. In a recent study, Chen and Yang (5) presented a systematic procedure for selecting a suitable calculation level and model structure for the application of the *ab initio* method to the graphite system. They concluded that the use of B3LYP/6-31G(d) model chemistry for molecular properties and of HF/3-21G(d) for stability and geometry optimization, using a seven-ring graphene layer, is the most suitable compromise between accuracy, relevance and computational cost. Thus, for example, they used this approach, coupled with the atoms-in-molecule method (see below), to arrive at the intuitively appealing (and obvious!?) conclusion that a relatively large negative charge exists on the "unbalanced graphite edge sites" which are the "[re]active sites for carbon gasification reactions."

Before attempting to theoretically analyze the interaction between a gaseous molecule (O_2, NO, CO_2, H_2O) and the carbon surface (6), it is useful -- and indeed probably necessary -- to evaluate the theory in terms of its consistency with some well known facts about the electronic structure and surface chemistry of graphene layers. At the same time, it is expected that such a theoretical analysis will clarify the details of this electronic structure and thus help in the quantification of gasification reactivity. In particular, the electron density at the edge sites and its changes with the concentration of heteroatoms is of immediate interest. The affinity of the carbon surface for an oxidizing gas is assumed to be dependent on this electron density at the free carbon sites.

The electron density of a molecule is a fundamental property in quantum chemistry, readily amenable to theoretical analysis. The classical Mulliken population analysis, which assigns atomic charges, though arbitrary, is implemented in most commercially available molecular modeling programs. Its results should be viewed with caution, however, because they are known to be dependent on the level of theory and the basis set used. In contrast, the more recent atoms-in-molecule (AIM) approach is claimed not to have this limitation.

In this study a comparison is thus made between the Mulliken population analysis and the AIM approach in their ability to evaluate the electron densities in graphene layers by considering 1-, 2- and 4-ring aromatics. Following the pioneering work of Coulson and coworkers (7), "we can, provisionally, neglect all inter-layer effects and consider only the single layers separately."

COMPUTATIONAL METHODS AND MODEL STRUCTURES

The Gaussian 98W software package (4,8) was used in most calculations. When deemed necessary, it was complemented by Hückel molecular orbital as well as semi-empirical analyses. Figure 1 summarizes the structures that were selected for closer scrutiny. Their selection is based on the following considerations. We agree with Chen and Yang (5) that saturation of the boundaries of these model structures is a crucial step in reactivity calculations for graphite and, especially so, for carbons whose crystallites are much smaller than those in graphite. However, the choice of free edge sites versus hydrogen-saturated sites should not be one of convenience (7); rather, it should attempt to reflect the by now well documented delicate balance between free sites, H-saturated sites and oxygen-saturated sites (9). A comparison of bond orders and charge distributions in structures 1-4 within each series will thus be of interest. Similarly, ever since the pioneering work of Coulson and coworkers (7,10), as well as that of Stein and Brown (11), it has been clear that the size of the graphene layer is an important variable to consider even when edge chemistry is of primary interest. More recent theoretical analyses of carbon gasification (2,3), as well as experimental studies of liquid-phase adsorption on carbons (9), have indeed suggested that the electron density in the basal plane of the graphene layer is affected in an important way by the presence of heteroatoms at the edges, and vice versa. It is thus necessary to assess the dependence of these electronic effects on the size of the graphene layers. A comparison of the bond orders and charge distributions in series B1-N1-P1, B2-N2a-P2a, B3-N3a-N3b-P3a-P3b-P3c, B4-N4a-N4b-P4a-P4b-P4c will make this possible in a first approximation. An additional benefit of analyzing model structures containing few rings is that the results (model structures B1, B3, N1, N3a, N3b, P1, P3a, P3b and P3c) can be readily compared with experiments. Since some "50 carbon atoms" which form a "condensed system with at least two, and preferably three, hexagons in each direction"(7) are thought to be necessary before the model system "may be regarded as graphite and not as a large molecule approximating to graphite"(7), in future work we shall analyze even larger heteroatom-containing graphene layers. For now, we focus on the electron density at the edge carbon atoms, since surprisingly few papers (12,13) have been devoted to this crucial issue for carbon gasification reactivity.

PRELIMINARY RESULTS AND DISCUSSION

Tables 1 and 2 summarize some of our preliminary results. A key unresolved issues is the degree of localization of carbon's π electrons during gasification reactions. In particular, if the localization of π electrons contributes to the stabilization of free edge sites, as has been argued elsewhere (9), then the resultant redistribution of charge density will produce changes in C–C bond lengths, thus affecting CO and/or CO_2 desorption, as well as changes in the affinity of edge sites toward reactant gas chemisorption. Indeed, Wiberg (14) recently used ab initio MO theory to conclude that π electron distribution in condensed aromatic systems is the dominant factor in determining bond lengths.

It is seen in Tables 1a and 2a (note the underlined values) that the presence of carbonyl oxygen produces a consistent increase in the C–C bond lengths adjacent to the C=O group. This in turn supports the concept of induced heterogeneity in carbon gasification kinetics (2,3). It is also interesting to note that the predicted adjacent bond weakening effects of chemisorbed oxygen are sensitive to both the concentration and the exact location of C-O surface complexes. Thus, for example, while bond C8–C9 in structure P3b is weaker than bond C9–C12, as intuitively expected, bond C6–C7 in structure P3a is not weaker than bond C7–C14.

Tables 1b and 2b show that the electron density distribution using the Mulliken population analysis must be subjected to close scrutiny. (The underlined values in Table 2b are the atomic charges on the edge carbon atoms.) While the C atoms adjacent to the carbonyl group are predicted to have a higher affinity for O_2, the electron density at other reactive sites may be lower.

To what extent these trends are affected, in quantitative and perhaps even qualitative terms, when more realistic edge saturation and molecular size effects are introduced, and how this can affect carbon gasification kinetics (15), is the subject of our continued studies.

Table 1a. Comparison of C–C bond lengths (Å) in 2-ring model structures using B3LYP/6-31G(d)//HF/3-21G* with Gaussian 98W.

	1–2	2–3	3–4	4–10	5–10	5–6	6–7	7–8	8–9	1–9
N1	1.357	1.414	1.357	1.419	1.419	1.357	1.414	1.357	1.419	1.419
N3a	1.323	1.475	1.477	1.330	1.466	1.323	1.475	1.477	1.330	1.466
N3b	1.479	1.473	1.326	1.461	1.336	1.459	1.328	1.472	1.495	1.327

Table 1b. Comparison of atomic charges in 2-ring model structures using B3LYP/6-31G(d)//HF/3-21G* with Gaussian 98W.

	C1	C2	C3	C4	C5	C6	C7	C8	C9	C10
N1	-.186	-.134	-.134	-.186	-.186	-.134	-.134	-.186	.131	.131
N3a	-.138	-.189	.448	-.305	-.138	-.189	.448	-.305	.182	.182
N3b	-.190	.503	-.271	-.169	-.216	-.219	-.258	.558	-.163	-.078

Table 2a. Comparison of C–C bond lengths (Å) in 4-ring model structures using B3LYP/6-31G(d)//HF/3-21G* with Gaussian 98W.

	1–10	10–12	9–12	8–9	8–14	7–14	6–7
P1	1.382	1.390	1.445	1.338	1.445	1.390	1.382
P3a	1.326	1.464	1.367	1.405	1.363	1.485	1.474
P3b	1.396	1.370	1.475	1.523	1.476	1.370	1.396
P3c	1.470	1.333	1.463	1.325	1.463	1.333	1.470

Table 2b. Comparison of atomic charges in 4-ring model structures using B3LYP/6-31G(d)//HF/3-21G* with Gaussian 98W.

	C1	C10	C12	C9	C8	C14	C7	C6
P1	-0.119	-0.230	0.161	-0.186	-0.186	0.161	-0.230	-0.119
P3a	-0.179	-0.157	0.167	-0.227	-0.185	0.048	0.390	-0.179
P3b	-0.121	-0.190	0.050	0.339	0.339	0.050	-0.190	-0.121
P3c	0.470	-0.343	0.238	-0.171	-0.171	0.238	-0.343	0.470

REFERENCES

1. L. R. Radovic, in *Encyclopedia of Materials: Science and Technology*. K. H. J. Buschow et al., Eds., Pergamon, Amsterdam, 2000, in press.
2. K. Skokova, L. R. Radovic, "On the role of carbon-oxygen surface complexes in the carbon/oxygen reaction mechanism," American Chemical Society, Div. Fuel Chem. Preprints, New Orleans (1996), p. 143.
3. K. A. Skokova, L. R. Radovic, in preparation (2000).
4. J. B. Foresman, A. Frisch, *Exploring Chemistry with Electronic Structure Methods*, Gaussian, Inc., Pittsburgh, 1996.
5. N. Chen, R. T. Yang, *Carbon* **36**, 1061-1070 (1998).
6. T. Kyotani, A. Tomita, *J. Phys. Chem. B* **103**, 3434-3441 (1999).
7. M. Bradburn, C. A. Coulson, G. S. Rushbrooke, *Proc. Royal Soc. Edinburgh* **A62**, 336-349 (1948).
8. M. J. Frisch et al., Gaussian, Inc., 1998.
9. L. R. Radovic, in *Surfaces of Nanoparticles and Porous Materials*. J. A. Schwarz, C. I. Contescu, Eds., Marcel Dekker, New York, 1999, pp. 529-565.
10. C. A. Coulson, L. J. Schaad, L. Burnelle, "Benzene to Graphite–The Change in Electronic Energy Levels," Third Biennial Conference on Carbon, University of Buffalo, Buffalo, NY, Pergamon Press, 1959, p. 27.
11. S. E. Stein, R. L. Brown, *J. Amer. Chem. Soc.* **109**, 3721-3729 (1987).
12. C. A. Coulson, "The electronic structure of the boundary atoms of a graphite layer," Fourth Conference on Carbon, University of Buffalo, Buffalo, NY, Pergamon Press, 1960, p. 215.
13. D. J. Klein, L. Bytautas, *J. Phys. Chem. A* **103**, 5196-5210 (1999).
14. K. B. Wiberg, *J. Org. Chem.* **62**, 5720-5727 (1997).
15. T. Kyotani, K.-I. Ito, A. Tomita, L. R. Radovic, "Monte Carlo Simulation of Carbon Gasification Using Molecular Orbital Theory," *AIChE J.* **42**, 2303-2309 (1996).

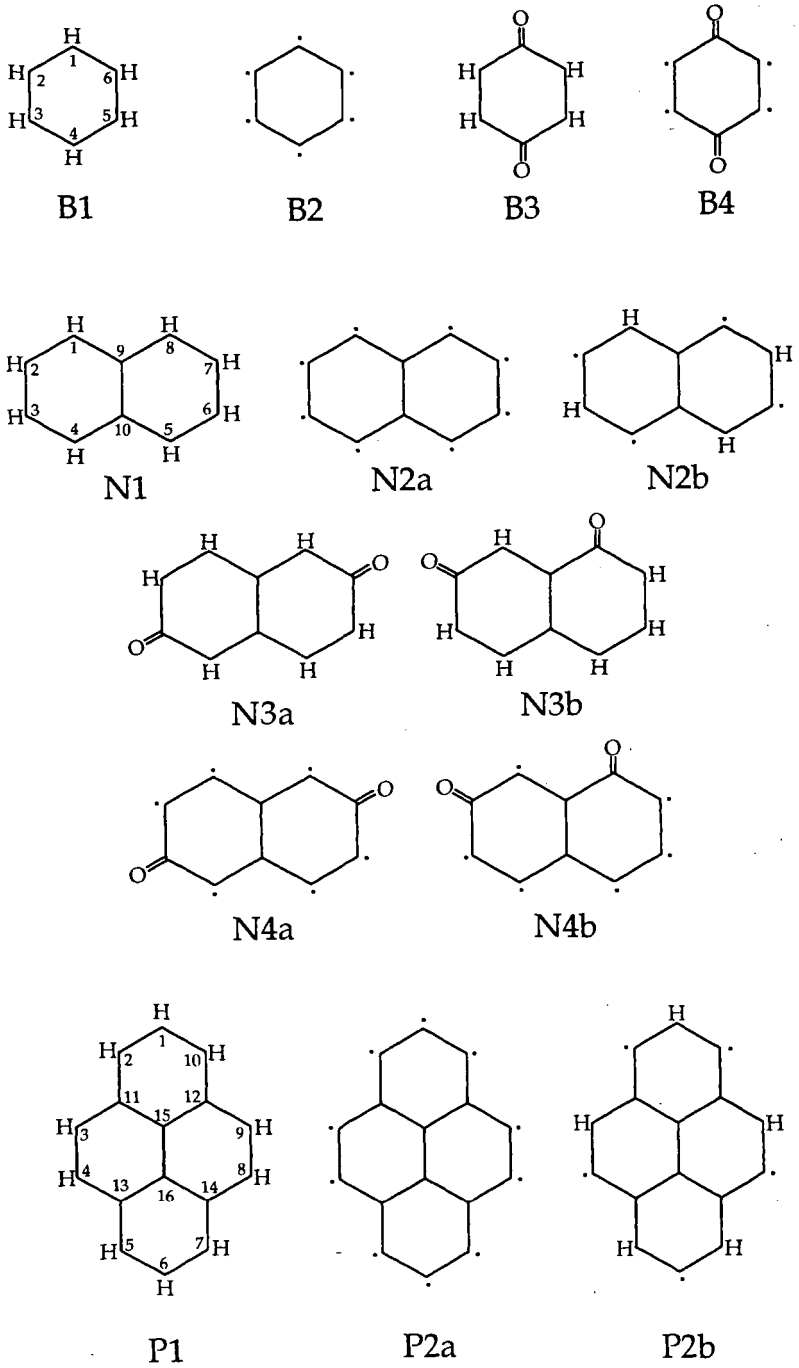

Figure 1. Model structures selected to represent the important surface chemistry effects in carbon gasification kinetics.

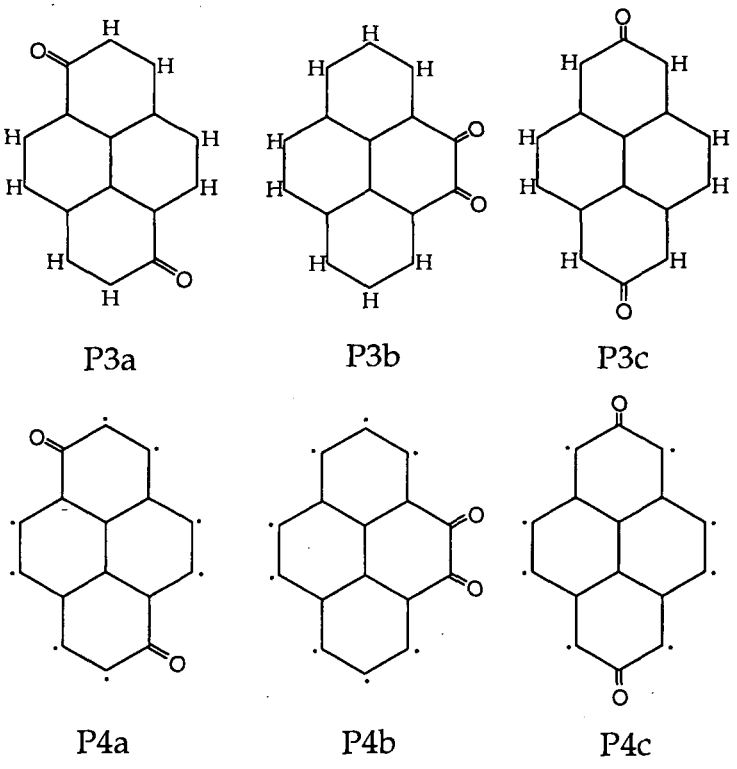

Figure 1 (continued). Model structures selected to represent the important surface chemistry effects in carbon gasification kinetics.

HYDROGENATION MECHANISM OF BENZYL ALCOHOL IN POLAR SOLVENTS ESTIMATED BY MO CALCULATION

Hideyuki Takagi, Takaaki Isoda, Katsuki Kusakabe and Shigeharu Morooka

Department of Materials Physics and Chemistry, Graduate School of Engineering,
Kyushu University, Fukuoka 812-8581, Japan

Key words: MO calculation, hydrogenation of benzyl alcohol in polar solvent, reaction coordinate

INTRODUCTION

The hydrogenation of aromatic structures is a key reaction in the hydrorefining of heavy oil, asphaltene and coal extracts. In previous studies,[1,2] we examined the hydrogenation of benzyl alcohol, which was the model compound as the coal extracts from low rank coal, over a ruthenium catalyst at 120°C in a variety of solvents. Our findings showed that the hydrogenation reactivity of benzyl alcohol was related to the relative permittivity of the reaction medium, but the mechanism was not clarified in detail.

Recently, the computer chemistry have been developed, and the structures of intermediates during the chemical reaction can be estimated by molecular orbital (MO) calculation using the personal computer.[3] In an earlier study,[4] we calculated changes in the reaction coordinates during the hydrogenation of benzene and found that the calculated activation energy agreed with that obtained experimentally. A conductor-like screening model (COSMO) assumes that the solvent is a homogeneous medium with a relative permittivity. The reaction coordinate for the hydrogenation of an aromatic compound in a polar solvent can be then analyzed via the application of the COSMO method to the MO calculation.

In the present study, benzyl alcohol was hydrogenated using a ruthenium catalyst at 120°C at a hydrogen pressure of 6 MPa in polar solvents. The reaction coordinate for hydrogenation of benzyl alcohol was estimated by MO calculation, in conjunction with the COSMO method, and the hydrogenation mechanism in polar solvents was discussed.

EXPERIMENTAL SECTION

Benzyl alcohol and ethanol were used as the substrate and the solvent, respectively. An alumina-supported ruthenium catalyst (Ru/Al_2O_3, Wako Chemical) was used as a hydrogenation catalyst. A typical reaction involved the use of 3 g of benzyl alcohol, 0.5 g of catalyst, and 6 g of ethanol. In order to vary the permittivity of the medium, a 3 g portion of formic acid or acetic acid was added. The relative permittivity of a mixed solvent, P_{mix}, can be calculated from the following equation.

$$P_{mix} = (P_iX_i + P_jX_j)/(X_i + X_j) \quad (1)$$

where P_i and P_j are the relative permittivities of solvent i and solvent j, respectively.[1] X_i and X_j are the mass fractions of solvent i and j, respectively, ($X_i + X_j = 1$). Table 1 shows the relative permittivity of solvents. All reactions were performed in a 50-mL batch autoclave at 120°C for 0-30 min under a hydrogen pressure of 6 MPa. After the reaction, the products were qualitatively and quantitatively analyzed by GC-FID (GC-14A, Shimadzu) and GC-MS (QP-5000, Shimadzu), equipped with a capillary column. Details of the reaction have been reported previously.[2] Reaction rate constants for the hydrogenation of benzyl alcohol in solvents were then determined from the yields of products.

SIMULATION

Figure 1 shows the pathways for reaction of benzyl alcohol over the Ru/Al_2O_3 catalyst.[1] Hydrogenation of the aromatic ring (route 1) and hydrogenolysis of hydroxy group (route 2) proceed competitively. Cyclohexanecarbaldehyde is produced via route 1, and toluene via route 2. Methylcyclohexane is produced via the hydrogenation of the produced toluene.

A molecular orbital (MO) calculation for hydrogenation of benzyl alcohol was carried out using WinMOPAC Vr.1 (Fujitsu) based on a PM3 Hamiltonian method, and the energy minimization

was defined by an EF method.[3] A hydrogen atom was coordinated to an optional atom located on benzyl alcohol or an intermediate molecule. The reaction coordinate between the hydrogen atom and the substrate was then calculated from 3 Å to 1 Å at a step of 0.1-0.2 Å using the COSMO method. The heat of formation was plotted against the reaction coordinate, and the activation energy was calculated as follows:

$$Ec = Et - Ep \quad (2)$$

where Ec is the activation energy. Et and Ep are the heat of formation of the transition complex and that of the initial or intermediate compound, respectively.

RESULTS

Hydrogenation via route 1

Figure 2 shows the relationship between the reaction rate constant of route 1 for the hydrogenation of benzyl alcohol at 120°C and the relative permittivity of the medium. The rate constant for route 1 was 8.2×10^{-4} s^{-1} with no solvent, and 4.5×10^{-4} s^{-1} in ethanol as the solvent. The addition of acetic acid led to a decrease in the relative permittivity of the medium, and an increase in the rate constant to 8.2×10^{-4} s^{-1}, which was equal to that for the reaction with no solvent. The hydrogenation was completely retarded by the addition of formic acid with a high relative permittivity. This indicates that the rate constant of route 1 can be related to the relative permittivity of the reaction medium.

Figure 3 shows the change in the reaction coordinate for the hydrogenation of benzyl alcohol via route 1. In step 1, the activation energy is 24.6 kcal/mol with no solvent (relative permittivity = 13.1), and 46.6 kcal/mol for the ethanol-formic acid solution (relative permittivity = 30.0). No activation energy is apparent for step 2. In step 3, the activation energy is 12.0 kcal/mol with no solvent, and 26.9 kcal/mol for the ethanol-formic acid solution. In addition, no activation energy is apparent for step 4. A hydrogen atom is not introduced into the double bond of 1-cyclohexanylmethanol, based on the MO calculation. This supports the experimental findings that 1-cyclohexanylmethanol was converted to cyclohexanecarbaldehyde.[1,5]

Figure 4 shows the activation energy in route 1 for the hydrogenation of benzyl alcohol as a function of the relative permittivity. The activation energy is determined as the sum of the values of steps 1 and 3. The activation energy is 49.9 kcal/mol for the hydrogenation in ethanol and is decreased to 43.9 kcal/mol by the addition of acetic acid with a low relative permittivity. On the other hand, the activation energy is increased to 73.5 kcal/mol by the addition of formic acid with a high permittivity. In the route for hydrogenation of the aromatic ring in benzyl alcohol, the activation energy, which is estimated from the MO calculation, decreases with decreasing

Table 1. Relative Permittivity of Solvents

system	composition in weight [g] (substrate:solvent:additive)	relative permittivity of mixed solvent
in vacuum		0.0
benzyl alcohol (no solvent)		13.1
ethanol	3 : 6	20.6
ethanol/acetic acid	3 : 6 : 3	17.0
ethanol/formic acid	3 : 6 : 3	30.0

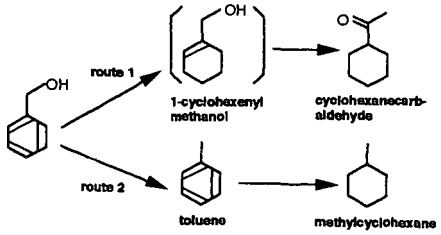

Figure 1. Pathways for reaction of benzyl alcohol over Ru/Al_2O_3 catalyst.

relative permittivity of the solution.

Hydrogenolysis via route 2

Table 2 shows the reaction rate constant for hydrogenation of benzyl alcohol via route 2. The rate constant at 120°C was 0.59×10^{-4} s^{-1} with no solvent, and remained unchanged after the addition of ethanol. The addition of acetic acid in ethanol lead to an increase in the rate constant to 1.57×10^{-4} s^{-1}. Figure 5 shows the hydrogenolysis reaction via route 2, as estimated by the MO calculation. A proton (H^+) is linked to the oxygen atom of the hydroxy group, and intermediate-1 is formed. However, hydrogen atom (H) cannot be attached to the hydroxy group nor the carbon atoms adjacent to the hydroxy group. Intermediate-2 is formed by the attack of a hydrogen atom and then is decomposed, producing toluene and water. This suggests that the hydrogenolysis of the hydroxy group

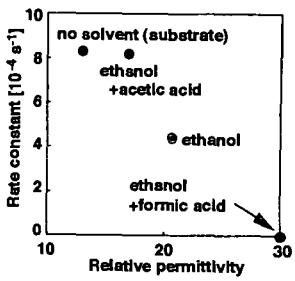

Figure 2. Relationship between reaction rate constant of route 1 for hydrogenation of benzyl alcohol 120°C and relative permittivity of medium.

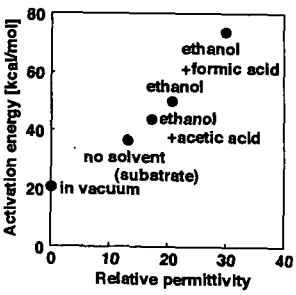

Figure 4. Activation energy in route 1 for hydrogenation of benzyl alcohol as a function of relative permittivity.

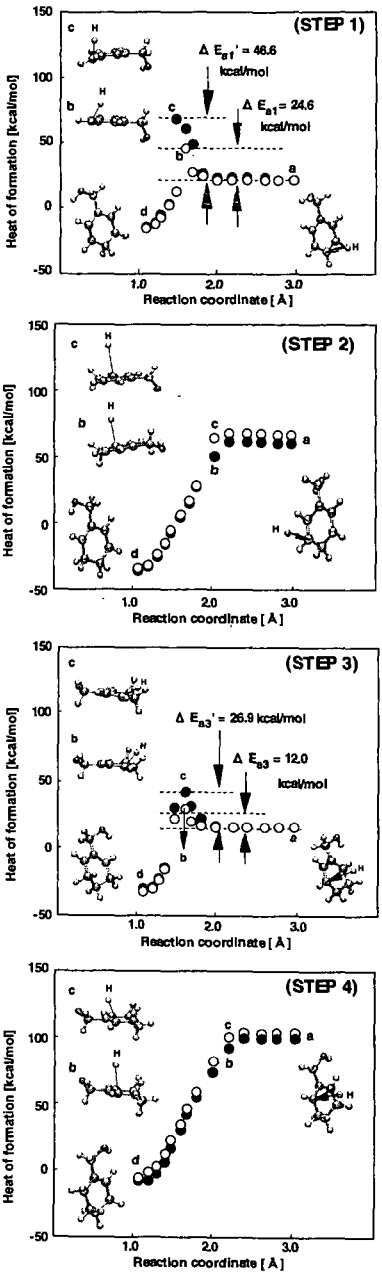

○ relative permittivity; 13.1
● relative permittivity; 30.0

Figure 3. Changes in reaction coordinate for hydrogenation of benzyl alcohol via route 1.

Table 2. Reaction Rate Constant for Hydrogenation of Benzyl Alcohol via Route 2

system	rate constant $[10^{-4}\ s^{-1}]$
benzyl alcohol (non-solvent)	0.59
ethanol	0.58
ethanol/acetic acid	1.57
ethanol/formic acid	0.0

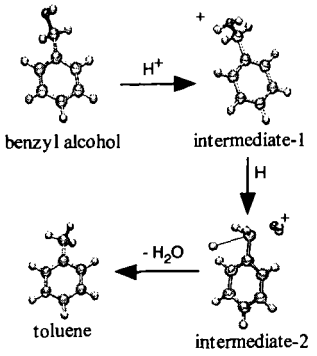

Figure 5. Hydrogenolysis reaction via route 2 estimated by MO calculation.

proceeds via an S_N2 mechanism.

DISCUSSION

The hydrogenation reaction of aromatic compounds with polar substituents, as well as benzyl alcohol, can be divided into two routes; hydrogenation of aromatic ring; and hydrogenolysis of oxygen-containing substituents and bridge bonds. As shown in Figure 2, the rate constant for hydrogenation of the aromatic ring, which was obtained by experimental results, increases with decreasing relative permittivity of the solution. The MO calculation indicates that the heat of formation for the transition state is dependent on the structure, which vary with the relative permittivity of the solution. The heat of formation for the transition state decreases with decreasing relative permittivity of the solution, and, as a result, the activation energy of route 1 decreases. This MO calculation suggests that the value of the heat of formation is related to the reaction rate of route 1. Present study also clarified that the hydrogenolysis of benzyl alcohol is an S_N2 reaction and is promoted by the donation of a proton from the solvent.

CONCLUSIONS

The reaction rate for route 1 increased with decreasing relative permittivity of the solution. The activation energy for hydrogenation of the aromatic ring in benzyl alcohol was estimated by an MO calculation, and decreased with decreasing relative permittivity of the reaction medium. Hydrogenolysis of the OH group in benzyl alcohol was promoted by donating a proton from the solvent, and was consistent with proceeding via an S_N2 reaction. The addition of acetic acid in ethanol enhanced the hydrogenation of the aromatic ring, as well as the hydrogenolysis of benzyl alcohol, but the addition of formic acid inhibited the catalyst activity. This concludes the role of the additives in hydrogenation of aromatic compounds with polar substituents.

ACKNOWLEDGMENT

This work was supported in part of by a "Research for the Future Project" grant from the Japan Society for the Promotion of Science (JSPS), through the 148th Committee on Coal Utilization Technology. Dr. Jerzy M. Rudziski and Ms. Mayumi Matsushita of Fujitsu Kyushu System Engineering Ltd., Japan, supported the computer software used in this study. Useful discussion with Dr. Keiichiro Samejima of Fujitsu Ltd., Japan is deeply acknowledged.

REFERENCES

(1) Takagi, H.; Isoda, T.; Kusakabe, K.; Morooka, S. *Energy Fuels* **1999**, *13*, in press.
(2) Takagi, H.; Isoda, T.; Kusakabe, K.; Morooka, S. *Prepr. Pap- Am. Chem. Soc., Div. Fuel Chem.* **1999**, *44*, 1029.
(3) Isoda, T.; Takase, Y.; Isumi, N.; Kusakabe, K.; Morooka, S. *J. Jpn. Pet. Inst.* **1998**, *41*, 318.
(4) Takagi, H.; Isoda, T.; Kusakabe, K.; Morooka, S. *Energy Fuels*, to be submitted.
(5) Nisimura, S.; Hama, M.; *Bull. Chem. Soc. Jpn.* **1966**, *39*, 2467.

The American Chemical Society Symposium on the Molecular Modeling of Solid Fuel Reactions, 219th ACS National Meeting, San Francisco, March 26-30, 2000

Analysis Of Initial Stage Reactions In Coal Pyrolysis By Molecular Orbital Calculation

Takaaki Isoda, Hideyuki Takagi, Katsuki Kusakabe and Shigeharu Morooka

Department of Materials Physics and Chemistry, Graduate School of Engineering, Kyushu University, Fukuoka 812-8581, Japan

INTRODUCTION

Pyrolysis of coal has been explained based on a chemical percolation and dissociation model [1]. In the early stage of pyrolysis, cross-link structures, which connect aromatic units, as well as peripheral groups, are cleaved, and radical fragments are produced. These radicals are rapidly stabilized to gases, tar and char. The overall pyrolysis reactivity is dependent on the structure of coal.

We recently reported, however, a combination of H_2O_2 oxidation in the presence of alcohols and hydrogenation of the ethanol-extracted samples using a Ru/Al_2O_3 catalyst can alter the coal structure and increase the pyrolysis reactivity. [2] When Yallourn coal was treated by the H_2O_2 oxidation in the presence of alcohols and by the hydrogenation at 120℃ for 12-72 h at a hydrogen pressure of 10 MPa, the char yield of flash pyrolysis was decreased from 50wt% for the raw coal to 25wt% for the treated coal [2]. Structural analyses of the hydrogenated coal indicated that aromatic rings of the raw coal were partially converted to saturated rings [3]. This indicates that the coal pyrolysis reactivity is also depended on the unit structure in the coal macromolecule.

In this study, pyrolysis reactivities, as well as product distributions, of raw coals was evaluated using a Curie-point pyrolyzer (CPP). The cleaving energies of unit structures of coal were estimated by a reaction coordinate analysis based on molecular orbital calculation. The coal pyrolysis reactivity was then discussed on the basis of the cleaving energy of unit structures.

EXPERIMENTAL SECTION

Pyrolysis; The elemental composition of the coal is summarized in Table 1. Yallourn (YL), South Banko (SB), Taiheiyo (TH), Miike (MI), and Hunter Valley (HV) coals were ground to give particles which were 37-74 μ m in size, and dried at 70℃ for 24 h prior to use. A coal sample of 1.5 mg was tightly wrapped with a ferromagnetic foil and pyrolyzed at 386-1040℃ using a Curie-point pyrolyzer, which could heat the sample at a heating rate of 3000 K/s. Produced gases were analyzed by GC-TCD and GC-FID. Details of the CPP were reported previously [4].

MO Calculation; The decomposition of unit structures of coals was simulated using WinMOPAC Vr.1 and 2 (Fujitsu), based on a PM3 Hamiltonian and an unrestricted Hartree-Fock method [5]. The unit structure of coal were assumed to be terminated with hydrogen atoms. The molecular weight of the unit structures were 370-398, depending

on coal ranks [6].

RESULTS AND DISCUSSION

Fig.1 shows the snapshots for the detachment of a methoxy group, which is substituted on the unit model structure of a low rank coal (YL). Fig.2 shows the changes in the heat of formation (H.O.F.), corresponding to Fig.1. The distance between the oxygen atom of the methoxy group and the carbon atom of the benzene ring is increased from position with a step of 0.1 Å. The H.O.F., which is E_a at position a, increases with increasing reaction coordinate, and the bond is cleaved at position b. The H.O.F. then approaches to a final value, E_c, when the reaction coordinate is over 2.5 Å [2]. Thus, the energy, which is required to cleave the bond, is calculated from

$$E_{cal} = E_c - E_a \quad (1)$$

where E_c and E_a are the H.O.F at the excited state (position c) and that at the ground state (position a), respectively. Tables 2-4 show the calculated cleaving energies. The numbers in the tables correspond to those in the unit structure models [6]. As shown in Fig.3, the cleaving energies are similar for the coal unit structure models, because the unit structures are not suffered by the effect of non-covalent bond and steric hindrance in the structure. The C=C double bond requires the largest cleaving energy, 420-470 kJ/mol. The cleavage of single bonds on the benzene ring, such as -OH, -Me, and -H groups, needs cleaving energies of 340-410 kJ/mol. This indicates that the elimination of hydroxy and methyl groups and hydrogen from the benzene ring is rather difficult during pyrolysis. However, the elimination of C-C and C-O bonds requires cleaving energies of 170-300 kJ/mol. The cleaving energy of a carboxy group from the benzene ring of the low rank coal is as low as 159 kJ/mol.

The pyrolysis of raw coals was initiated at 350℃, and the coal conversion increased with increasing temperature in the range of 500-800℃. Fig.4 shows the effect of the reaction temperature on the yields from the flash pyrolysis of the YL coal. The temperature effect can be described by the enthalpy, Q_c, which the coal sample attains during the heating from the initial temperature, T_1, (50℃) to the reaction temperature, T_2. Assuming that the heat capacity of the coal sample, C_p, is constant in the temperature range, the enthalpy can be described as follows:

$$Q_c = C_p(T - T_1) \quad (2)$$

where Q_c and C_p are expressed based on the mole of carbon in the raw coal. The enthalpy was 6.3-23.3 kJ/mol-C under the present experimental conditions.

As shown in Fig.4, the yield of CO_2 was increased at Q_c = 8-9 kJ/mol-C. This is ascribed to the decomposition of carboxy (C·COOH) and methoxy (O·Me) groups. Methylene cross-links (methylene C·C), C-C and C-H single bonds in naphthenic rings (cyc C·C and cyc C·H) may be cleaved in the range of 10-15 kJ/mol-C. The detachment of hydrogen from methyl groups (H.·CH2-) and that of methyl groups (C·Me) also proceeds in this enthalpy range, and the yields of tar and hydrocarbon gases were increased. Double bonds on the aromatic rings (benzene C=C) were cleaved above 450 kJ/mol on the MO calculation, as well as high temperature, whereas the coal conversion was mostly saturated above 20 kJ/mol-C. The coal is then converted to char, which was stable at high temperatures.

Fig.5 shows the yield of total volatile matter, TVM, from pyrolysis of coals of

different ranks. The TVM from the low-rank and subbituminous coals was increased in the range of Q_c > 10 kJ/mol-C, and the pyrolysis reactions are ascribed to the decomposition of carboxy and methoxy groups. However, the TVM from the bituminous coals is increased in the range of 10-17 kJ/mol-C and is mostly composed of tar. In this energy range, cross-links were cleaved, and hydrogen was detached, radicals were effectively stabilized by the hydrogen transfer mechanism, and tar was formed. The above experimental results are in agreement with the order of the calculated cleaving energies shown in Fig.3. The pyrolysis reactivity of coal is decided by parallel radical reactions, of which the activation energies are lower than the cleaving energies. Thus, the activation energies for pyrolysis cannot be directly compared to the cleaving energies calculated by the MO calculation. Under the present pyrolysis conditions, however, the pyrolysis reactions occurred in the range of Q_c = 7-20 kJ/mol-C. These values are equivalent to approximately 1/20 of the calculated cleaving energies.

LITERATURE CITED

[1] Grant, D.M.; Pugmire, R.J.; Fletcher, T.H.; Kerstein, A.R. *Energy Fuels* **1989**, *3*, 175.

[2] Isoda, T.; Takagi, H.; Kusakabe, K.; Morooka, S. *Energy Fuels* **1998**, *12*, 503.

[3] Takagi, H.; Isoda, T.; Kusakabe, K.; Morooka, S. *Int. Conf. Coal Sci.* **1999**, *Vol.1*, p.255.

[4] Hayashi, J.-i.; Mizuta, H.; Kusakabe, K.; Morooka, S. *Energy Fuels* **1994**, *8*, 1353.

[5] Hirano,T.; Tanabe, K.; *Mopac Guide Book*, Kaibunshodo, Tokyo, 1991.

[6] Murata, S.; Miura, M.; Nomura, M.; Takanohashi, T.; Iino, A.; Kumagai, H.; Sanada, Y.; Nakamura, K.; *J. Jpn. Inst. Energy* **1995**, *74*, 342.

[7] Hirano,T.; *Chemical Review*, **1998**, *5*, 19.

Acknowledgements. Dr. Jerzy M. Rudziski and Ms. Mayumi Matsushita of Fujitsu Kyushu System Engineering Ltd., Japan, supported the computer software used in this study. Useful discussion with Dr. Keiichiro Samejima of Fujitsu Ltd., Japan is deeply acknowledged.

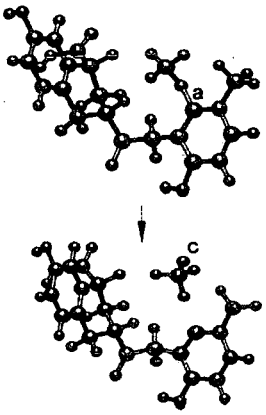

Fig.1 Detachment of a methoxy group from the unit structure model of low rank coal. (Reaction coordinate; a 1.3 Å, c 4.0 Å)

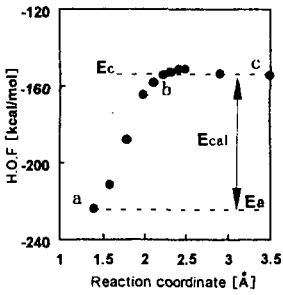

Fig.2 Changes in the heat of formation for detachment of a methoxy group from the unit structure model of low rank coal. Positions a and c correspond to those in Fig.1.

Table1 Elemental Composition of Coals

coal (abbreviation)		elemental analysis [wt%-daf] C	H	N	(O+S)[a]	ash
Hunter Valley	(HV)	80.6	5.5	2.1	11.8	9.5
Miike	(MK)	77.9	6.3	1.2	14.6	16.1
Taiheiyo	(TH)	73.8	6.6	1.2	18.4	10.9
South Banko	(SB)	68.5	5.4	1.2	24.8	2.0
Yalloum	(YL)	60.4	5.0	0.5	34.1	1.2

[a] determined by reference

Table 2 Cleaving Energies of Bonds in the Unit Structure Model of Low Rank Coal.

bond	position	cleaving energy [kJ/mol]
C-OMe	1	295
O-Me	2	170
C-Me	3	340
C-OH	4	391 - 394
CO-H	5	395
H_2C-H	6	295 - 318
benzene-H	7	386 - 416
CO-OH	8	340
C-COOH	9	159
methyleneC-C	10	163 - 320
cycC-C	11	233 - 291
benzeneC=C	12	422 - 474
cycC-H	13	260-306

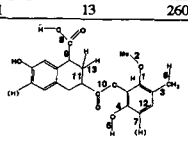

Table 3 Cleaving Energies of Bonds in the Unit Structure Model of Subbituminous Coal.

bond	position	cleaving energy [kJ/mol]
C-Me	1	343
H-CH_2-	2	320
C-OH	3	376
H-OC-	4	262
H-CH-	5	257
benzene-H	6	385
C-O	7	189
methyleneC-C	8	227
benzeneC=C	9	448
2benzene-C	10	307
2benzeneC=C	11	469

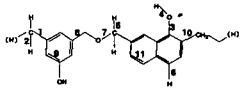

Table 4 Cleaving Energies of Bonds in the Unit Structure Model of Bituminous Coal.

bond	position	cleaving energy [kJ/mol]
C-Me	1	341
C-OH	2	389
H-OC-	3	288
H-CH_2-	4	298
benzene-H	5	407
H-CH-	6	279
C-O	7	169
methyleneC-C	8	243
2benzeneC=C	9	457
3benzeneC=C	10	395

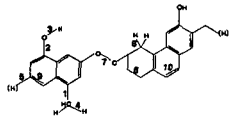

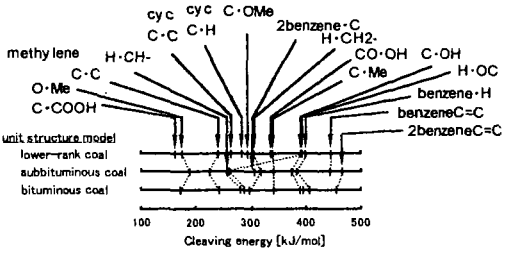

Fig.3 Cleaving energies for the unit structure models.

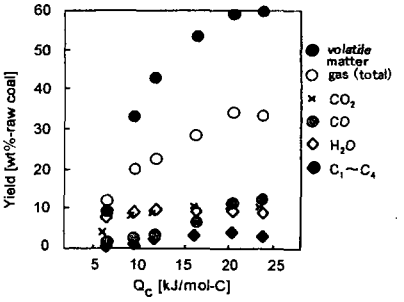

Fig.4 Effect of enthalpy changes for 1mol of raw coal carbon, Q_C, on product yields by pyrolysis of YL coal.

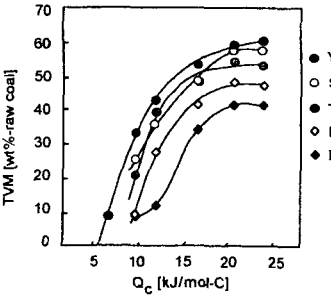

Fig.5 Effect of enthalpy changes for 1mol of raw coal carbon, Q_C, on the yield of total volatile matter by pyrolysis of coals.

MODELING OF MOLECULAR STRUCTURE OF UPPER FREEPORT COAL BY USING ^{13}C NMR CHEMICAL SHIFT CALCULATION

Toshimasa Takanohashi* and Hiroyuki Kawashima
Energy Resources Department, National Institute for Resources and Environment,
Tsukuba 305-8569, JAPAN

KEYWORDS: coal; model structure; ^{13}C NMR

INTRODUCTION

Many analytical techniques have been widely applied to structural analysis of coal. Solid-state ^{13}C NMR is one of the attractive tools for characterization of coal since coal is hard to dissolve in ordinary organic solvents. Recently, ^{13}C NMR chemical shift prediction software has been used to obtain information of chemical structure of various materials such as polymers. Thomas et al. calculated ^{13}C chemical shift for some substituted pyridines using several NMR prediction programs and showed that the results of the prediction gave good agreement with the experimental values[1].

Several structural models for coal have been based on analytical data obtained with the methods such as pyrolysis GC-MS, ^{13}C NMR measurement[2-4] and hydrogenation HPLC/GC-MS[5]. However, original structures of coals may be broken by pyrolysis and hydrogenation reactions, and only volatile materials of coals may be detectable on the GC techniques. On the other hand, for extract fractions obtained from a room temperature extraction for Upper Freeport coal, the model structures based on the structural parameters obtained from ^{1}H NMR and ultimate analysis were constructed[6]. Since no significant reaction such as bond breaking seemed to occur during the extractions, model structures based on original chemical structures could be constructed. However, information of types of carbon atom in the extract fractions was insufficient with ^{1}H NMR, and furthermore the model structure for the extraction residue could not be obtained, since it was insoluble in solvents.

To get directly information of chemical structures of a whole coal including the extraction residue, solid state ^{13}C NMR spectra were measured for several fractions which were obtained from extraction and fractionation at room temperature. The calculated ^{13}C NMR spectra by using an NMR prediction software were determined[7] for the model structures of the extract fractions that have been suggested by Takanohashi and co-workers[6]. The model structures were improved to fit experimental spectra. In addition, a model structure of the extraction residue was constructed and revised by comparison between its calculated ^{13}C NMR spectrum and the experimental one. Finally, a model structure of Upper Freeport coal including the extraction residue is suggested.

EXPERIMENTAL

Sample Preparation

Upper Freeport coal, which is an Argonne premium coal sample was obtained in ampoules (5 g of -150 μm)[8]. The coal sample was extracted exhaustively with a carbon disulfide / *N*-methyl-2-pyrrolidinone (CS_2 / NMP) mixed solvent at room temperature[9]. The extract obtained was further fractionated by acetone and pyridine into three fractions, acetone-soluble (AS), acetone-insoluble and pyridine soluble (PS), and pyridine-insoluble (PI) fractions, as shown in Figure 1. The PS, PI and residue (the mixed solvent-insoluble (MI) fraction) were washed with acetone, and the AS was washed with acetone – water (1:4 by volume) solutions. All fractions were dried in a vacuum oven at 80 °C for 12 hr.

NMR measurements

Solid state ^{13}C NMR spectra were measured by both CP/MAS and SPE/MAS methods using a Chemmagnetics CMX-300 NMR spectrometor operating at a ^{13}C frequency of 75.46 MHz. All spectra were acquired employing a ^{1}H 90 ° pulse length of 4 μs. This was combined with a magic angle spinning rate of 10kHz. Repetition rates of 4s (CP/MAS) and 60s (SPE/MAS) were used

for all samples. For each spectrum, 4000 (CP/MAS) and 2000 (SPE/MAS) scans were accumulated. The contact time of CP/MAS was 1ms. The chemical shifts were calibrated with respect to tetramethylsilane using the peak of methyl group on hexamethylbenzene at 17.4 ppm as the external standard.

NMR chemical shift calculation

Chemical shift calculations were carried out using a ACD laboratory C NMR predictor software. The software allows treatment of molecules containing up to 256 carbon atoms. The chemical shift of model structure is calculated by searching for similar sub-structural fragment with the corresponding experimental shift value in the database (600,000 chemical shifts of 50,000 compounds) and evaluating the chemical shift value taking into account intramolecular interactions. The calculated ^{13}C NMR spectra of the model structures for the fractions were obtained by considering an adequate line width.

RESULTS AND DISCUSSION

NMR spectra.

The distributions of types of carbon atom obtained by deconvolution of 13C NMR spectra for each fraction are shown in Figures 2. For all spectra, SPE/MAS gave the lower ratios of CH_3, CH_2, CH carbon and higher ones of aromatic and CH_2-O- carbon than CP/MAS. This is explained by that carbons with low CP efficiency such as non-protonated aromatic ones could be detected by SPE/MAS. Thus, for samples including many inner carbons like coal, SPE/MAS method may give more quantitative spectrum, although there are other problems such as background of spectrum. While, compared among fractions, the lighter fraction gave larger differences between both methods. Furthermore, the SPE/MAS data showed that except for AS fraction that is the lightest of all fractions here, all fractions including the extraction residue gave a similar distribution of carbon types. Nakamura et al. analyzed aromatic structures of several fractions obtained from mild hydrogenation and reported that ring structures for all fractions including an extraction residue were similar[5]. Iino et al. have also found[10] that addition of small amount (1%) of tetracyanoethylene (TCNE) to the CS_2/NMP mixed solvent enhanced greatly the extraction yield of Upper Freeport coal, i.e., the original MI became part of the PI fraction, and concluded that the effect of TCNE addition is attributed to dissolution of associates of the coal molecules. Therefore, the PS, PI and extraction residue (MI) have similar chemical structures and their difference may be due to the degree of association between coal molecules.

NMR Chemical Shift Calculation.

The model structures for AS, PS and PI fractions based on the structural parameters obtained from ^1H NMR and ultimate analysis have been suggested[6]. The calculated spectra for their model structures were obtained by using the prediction software. Next, the model structures were modified to fit the experimental spectra. Consequently, the modified model structures were obtained as shown in Figure 3. The calculated spectra of the modified models were compared with the experimental ones, which are shown in Figure 4. For all fractions, the calculated spectra were in excellent agreement with the experimentally obtained spectra. Table 1 shows ultimate analyses and structural parameters of each model, together with their experimental values. For AS fraction, which is the lightest of all fractions, there were differences in ultimate analysis. The model of AS fraction can be too small to express distribution of chemical structures. While, for PS, PI and MI, their ultimate analyses and structural parameters except for aromaticity, f_a were in good agreement with those of model. The f_a values of models except for AS were higher than those estimated from ^{13}C NMR and ^1H NMR measurements. This reason may be attributed to the inner carbons existed in the heavier fractions, which are hard to be relaxed even under SPE/MAS condition.

A Model Structure of Upper Freeport Coal.

Nakamura et al. constructed[5] three-dimensionally a model structure of Zao Zhuang bituminous coal using computer-aided molecular design (CAMD) by assuming an anisotropic model structure formed from a periodic boundary cell. The same method was used to construct a model structure of Upper Freeport coal here since both coals have similar structural features[9]. The modified model structures for all fractions including the extraction residue were randomly placed in a rectangular cell, as shown in Figure 5. It is not required to connect between the models by covalent bonds, because all fractions were obtained from the room-temperature extraction and fractionation. The calculation procedure has been reported elsewhere[5]. Finally an associated model structure of Upper Freeport coal was suggested. The estimated density for the model structure was in agreement with the observed one.

CONCLUSIONS

Upper Freeport coal was extracted and fractionated at room temperature, and for all fractions including the extraction residue, ^{13}C NMR spectra were measured. The calculated ^{13}C NMR spectra by using an NMR prediction software were determined for the model structures. The model structures were modified to fit experimental spectra. For all fractions, the spectra calculated for the modified models were in excellent agreement with the experimentally obtained spectra. Finally, by using computer-aided molecular design (CAMD), a anisotropic model structure of Upper Freeport coal was suggested.

ACKNOWLEDGMENT

This work has been carried out as one of "Research for the Future" projects of the Japan Society for the Promotion of Science (JSPS) through the 148th committee on coal utilization technology of JSPS.

REFERENCES

1) Thomas, S.; Bruhl, I.; Heilman, D.; Kleinpeter, E. *J.Chem.Int.Comput.Sci.* **1997**, *37*, 726.
2) Nomura, M.; Matsubayashi, K.; Ida, T.; Murata, S. *Fuel Proc. Tech.* **1992**, *31*, 169.
3) Hatcher, P.G.; Faulon, J.-L.; Wenzel, K.A.; Cody, G.D. *Energy Fuels* **1992**, *6*, 813.
4) Faulon, J.-L.; Hatcher, P.G.; Carlson, G.A.; Wenzel, K.A. *Fuel Processing Technology* **1993**, *34*, 277.
5) Nakamura, K.; Takanohashi, T.; Iino, M.; Kumagai, H.; Satou, M.; Yokoyama, S.; Sanada, Y. *Energy Fuels* **1995**, *9*, 1003.
6) Takanohashi, T.; Iino, M.; Nakamura, K. *Energy Fuels* **1998**, *12*, 1168.
7) Kawashima, H.; Takanohashi, T. *Prepr.Pap.-Am.Chem.Soc., Div.Fuel Chem.* **1999**, in press.
8) Vorres, K.S. *Energy Fuels* **1990**, *4*, 420.
9) Iino, M.; Takanohashi, T.; Obara, S.; Tsueta, H.; Sanokawa, Y. *Fuel* **1989**, *68*, 1588.
10) Liu, H.-T.; Ishizuka, T.; Takanohashi, T.; Iino, M. *Energy Fuels* **1993**, *7*, 1108.

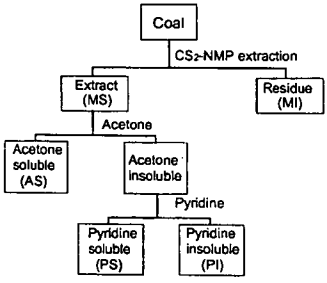

Figure 1 Procedures of Extraction and Fractionation

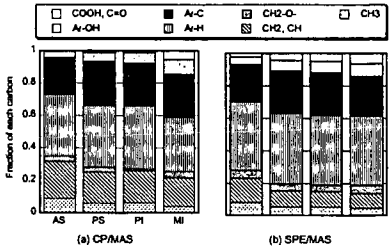

Figure 2 Solid state 13C NMR spectra of the fractions (AS, PS, PI and MI) by CP/MAS (a) and SPE/MAS (b) methods.

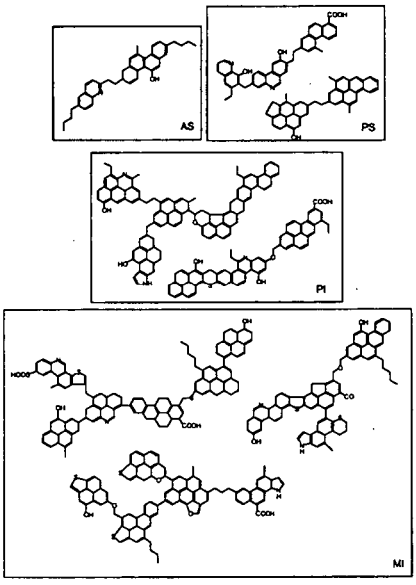

Figure 3 Modified Model Structures of Each Fraction

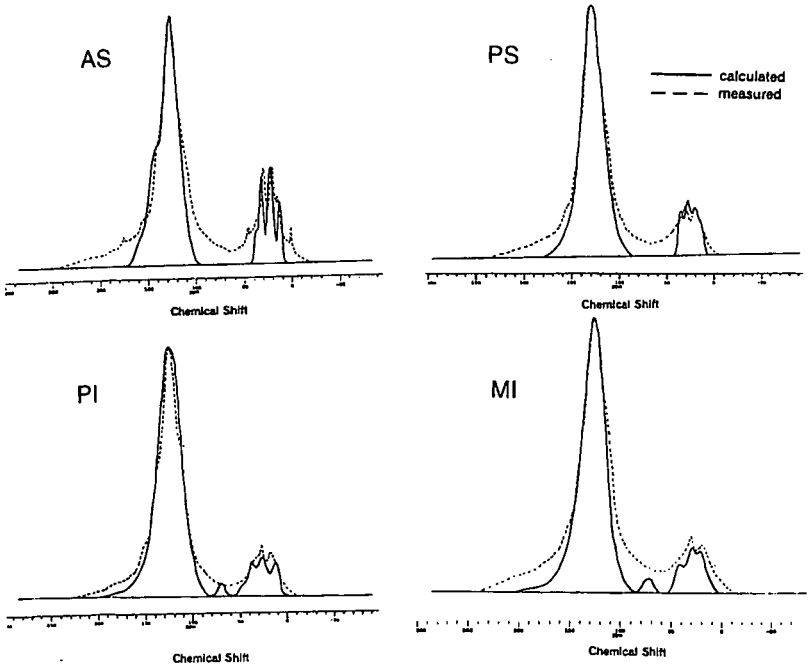

Figure 4 The measured ^{13}C NMR spectra for all fractions, and their calculated spectra.

Table 1 Ultimate Analyses and Structural Parameters for Each Fraction

fraction	C%	H%	N%	S%	O%	*H/C*	f_a[a]
AS, observed	88.5	6.7	1.1	0.5	3.2	0.91	0.72 (0.71)
model	86.9	7.4	2.7	0.0	3.0	1.03	0.71
PS, observed	86.6	5.4	1.8	1.0	5.2	0.75	0.80 (0.78)
model	85.6	5.5	2.3	0.0	6.6	0.77	0.84
PI, observed	85.8	5.0	2.1	1.1	6.0	0.68	0.81 (0.79)
model	85.7	5.0	2.0	1.5	5.9	0.70	0.85
MI, observed	81.7	4.7	1.8	5.5	6.3	0.69	0.81
model	81.8	4.9	1.7	5.4	6.2	0.71	0.85

[a] The values in parenthesis are calculated from ^{1}H NMR measurement.

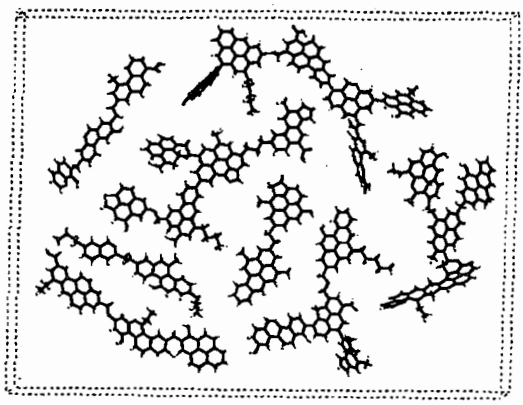

Figure 5 Coal Molecules Put Randomly in a Rectangular Cell.

CHARACTERIZATION OF CHARS FROM PYROLYSIS OF CHLOROGENIC ACID

Ramesh Sharma, Mohammad Hajaligol, Pamela Martoglio-Smith, and Jan Wooten
Philip Morris U.S.A., Research Center, P.O. Box 26583, Richmond, VA 23261

KEYWORDS: char, characterization, chlorogenic acid, combustion, pyrolysis

INTRODUCTION

Chlorogenic acid is a plant material that contains both phenolic and saccharide groups and can be a good representative model compound for biomass. It is one of the components of coffee seeds and tobacco leaves. Commercially, chlorogenic acid is extracted from coffee seeds. When pyrolyzed, chlorogenic acid is reported to undergo a rapid decomposition to form a gaseous product and a solid char. The char then undergoes further reactions to form additional product [1]. A number of studies are reported in the literature on the composition of the gaseous product from chlorogenic acid. Zane and Wender [2] heated a sample of chlorogenic acid in a flask at 600°C for 5 min and observed catechol, 4-methyl catechol, 4-ethyl catechol, benzoic acid, and quinide as the main components. Sakuma *et al.* [1] reported, in addition, phenol and 4-vinyl catechol. Schlotzhauer *et al.* [3] pyrolyzed chlorogenic acid at 800°C and observed 5-hydroxymethyl furfural in addition to the above products. These studies indicate that the composition of the gaseous product is dependent on the pyrolysis conditions. Although considerable work has been done on the analysis of the gaseous product, there is no information in the literature on the nature and composition of the product char or the effect of pyrolysis conditions on char characteristics. The nature of the char may govern the extent of secondary reactions.

In this work, the effect of pyrolysis conditions on the yield and nature of chars from chlorogenic acid was studied. The chars were produced at atmospheric pressure under oxidative and non-oxidative (inert) atmospheres and at temperatures ranging from 250° to 750°C. The non-oxidative runs were made with helium as the carrier gas; the oxidative runs with a mixture of 2% oxygen in helium. The concentration of oxygen in the oxidative runs was kept low to prevent a complete combustion of the substrate. The uncondensed gaseous product was analyzed by mass spectrometry. The product char was characterized in terms of its elemental analysis and surface area and by solid-state ^{13}C nuclear magnetic resonance (NMR) spectroscopy and Fourier-transform infrared (FTIR) spectroscopy. The surface morphology of char was studied by scanning electron microscopy (SEM). The results of char characterization are discussed in relation to the evolved gases.

EXPERIMENTAL

Chlorogenic acid was obtained from Fisher Scientific. It is predominantly the *trans* isomer with 99% purity. The pyrolysis reactor was a ½" diameter quartz tube heated by a 6" long metal-block furnace. The furnace provided about 4" length of uniform temperature profile. The runs were made at atmospheric pressure and temperatures ranging from 250° to 750°C. Up to 300 mg of chlorogenic acid was pyrolyzed in each run which lasted 10 min. The carrier gas was passed continuously over the sample at a flow rate of 220 ml/min. A sample of the uncondensed gaseous product was analyzed on-line by a Balzer QMG511 quadrupole mass spectrometer.

The elemental analysis of the product char was performed at Galbraith Laboratories, Inc. The BET surface area was measured in automated volumetric gas adsorption apparatus (Autosorb 1 from Quantachrome Co.) using nitrogen as an adsorbate. The ^{13}C CPMAS NMR spectra were obtained on a Varian Unity 200 spectrometer at a carbon resonance frequency of 50.3 MHz. The MAS spinning speed was ~8100 Hz. The infrared spectra were recorded on a Spectra-Tech IR-Plan microscope interfaced to a Nicolet Magna 560 FTIR spectrometer. The sample was mounted between two KBr plates held in a micro-compression cell. For the SEM analysis, a Topcon SM720 Field Emission Scanning Electron Microscope was used.

RESULTS AND DISCUSSION

Char Yield

Figure 1 shows the effect of temperature on the yield of the solid product, *i.e.* char yield, from chlorogenic acid. In non-oxidative runs, the yield decreases with increase in temperature from 80% at 250°C to 20% above 600°C. The oxidative runs (with 2% oxygen in helium) result in char yields which, at low temperatures, are virtually identical to those from the non-oxidative pyrolysis but are lower (than in non-oxidative runs) at high temperatures. Above 550°C, virtually all the char was converted to gaseous product in the oxidative runs. Interestingly, the char yields are not dependent on the mass of chlorogenic acid pyrolyzed. This indicates that the pyrolysis reactions may not be transport-limited under the pyrolysis conditions used in this study. A preliminary analysis of the data indicated activation energy of 40 kJ/mol for the non-oxidative pyrolysis and 300 kJ/mol for the oxidative pyrolysis. The activation energy for non-oxidative

pyrolysis is rather low. On the other hand, the activation energy for oxidative pyrolysis is typical of that associated with the char oxidation. The gaseous product consisted mainly of phenol, catechol, benzene, and benzoic acid in addition to water, CO and CO_2. Similar products are reported in the literature [2,3]. Above 600°C, in this study, the gaseous product also contained significant hydrogen.

Char Characterization

The product char was obtained as a volcano-like cone having a smooth and 'glassy' external surface. This indicates that the chlorogenic acid forms a melt at relatively low temperature, which is consistent with its melting point (208°C). SEM analysis of chars indicated that the decomposition of chlorogenic acid was accompanied by the formation of bubbles in the melt. The bubbles grew as the reaction proceeded until they broke allowing the gaseous products to escape. The formation, growth, and breaking of bubbles and, in turn, the evolution of the gaseous product and char, were controlled by the pyrolysis conditions. At low temperatures, the char particles were of irregular appearance with a few bubbles inside. At higher temperatures, the particles became more rounded and the bubbles grew larger and, in some cases, the bubble film was broken probably by the escaping gases which may have been released into another closed bubble or to outside. The surface of the melt became increasingly rough due to the growth of globular, rod-like, and platelet structures which decomposed further to leave a carbonized frame of bubbles and pores. Figure 2 shows a typical SEM micrograph of the surface of the char at 650°C. Some of the bubbles are seen to be intact. The char is almost completely carbonized at this temperature. In the presence of oxygen, these carbonized structures were oxidized completely above 550°C.

The hydrogen/carbon (H/C) and oxygen/carbon (O/C) ratios for the chars at different temperatures are plotted in Figure 3. Both the ratios decrease sharply with increase in the pyrolysis temperature indicating that the char becomes increasingly more carbonaceous in nature at high temperatures. Further, the H/C ratio decreases almost linearly with the decrease in the O/C ratio until about 650°C. The major reactions at these temperatures appear to be the dehydration and decarboxylation reactions. However, above 650°C, the H/C ratio drops dramatically relative to O/C ratio indicating a direct dehydrogenation of the product char. This is consistent with the analysis of the gaseous product. Interestingly, the use of oxidative atmosphere does not alter the H/C and O/C ratios significantly relative to those in the non-oxidative case at the same temperature. This may be due to the low concentration of oxygen in the carrier gas.

The BET surface area measurements indicated that the chars prepared below 550°C had a negligible surface area but that the area increased dramatically to 196 m^2/g at 650°C, before decreasing slightly at 750°C. Thus, the use of high temperatures seems beneficial in creating a char with a high surface area. The presence of oxygen also enhanced the surface area to a maximum of 90 m^2/g at 450°C. Thus, the presence of oxygen appears to affect the physical characteristics of char.

The solid-state ^{13}C CP/MAS NMR spectra of chars are presented in Figure 4. The multiplicities of resonances in the individual groups of peak are due to multiple crystalline modifications and/or multiple molecules in the crystalline lattice. The spectrum for chlorogenic acid (not shown) indicated that the chlorogenic acid is mainly crystalline in nature and contains aliphatic, aromatic, phenolic, carbonyl, and carboxyl structures. The spectra of chars (Figure 4) differ progressively with temperature from that of the chlorogenic acid. At 250°C, the resonance bands tend to be broad indicating an increase in the amorphous nature of the sample compared to chlorogenic acid. Since the resonance bands do not change appreciably in number or intensity, the changes appear to be mostly due to melting and the formation of an amorphous state. Above 250°C, there is a steady loss of oxygen functionality indicated by the loss of carbonyl absorptions. The spectrum for the 350°C char shows that the phenolic, carboxyl and carbonyl groups are still present, although the concentration of the latter two groups is considerably small. It is believed that the aliphatic and oxygen groups create links and loops between aromatic clusters of various sizes [4]. As the temperature is increased further, the char looses its aliphatic character completely and becomes more and more aromatic in nature. The resonance bands corresponding to carbonyl groups disappear mostly. The resonances corresponding to phenolic groups also decrease progressively in intensity until they become almost totally absent in the 650°C char. The oxygen-bonded carbons are no longer distinguishable and only a very small aliphatic peak remains, indicating a complete carbonization of the char. The char at 750°C could not be analyzed due to its high conductivity. Essentially similar observations were made from the NMR analysis of the oxidative chars, suggesting that many of the carbons in the chars that react with oxygen were lost probably by oxidation. These results appear to be at variance from those for chars prepared from cellulose [5] where it was observed that the aliphatic resonance of the char was significantly reduced while the resonance of aromatic carbons bonded to oxygen

increased. The difference could be due to differences in substrates as well as in pyrolysis conditions.

The FTIR results, presented in Figure 5, also suggest large chemical changes in chlorogenic acid above 250°C. Both the hydroxyl and carbonyl groups are gradually lost as the pyrolysis temperature is increased although the loss in hydroxyl groups does not appear to be as rapid as that in the carbonyl groups. The aliphatic character of char also decreases at high temperatures. On the other hand, the aromatic character, the C=C and the aromatic ring activities increase and are highest at 650°C. At 750°C, all the bands due to OH, CH, CH_2, and CH_3 stretches have vanished and there is a weak band for C=O. The char is mainly an aromatic polymer of carbon atoms. The spectra show an increasingly large drift in the baseline at high temperatures, which could be due to increase in the carbon black-content of the char as a result of increased carbonization. Boon *et al.* [6] observed a similar loss of oxygen functionality and an increase in the aromatic character with the cellulose chars at high temperatures. As in NMR analysis, the FTIR analysis showed essentially no effect of oxygen on the char characteristics.

The results of characterization are consistent with the evolution of the gaseous products. As the pyrolysis temperature is increased, the char looses most of its oxygen and hydrogen to the gaseous products such as water, CO, and CO_2, and becomes more carbonaceous in nature and low in crystallinity. The char probably also undergoes a direct dehydrogenation at high temperatures.

CONCLUSIONS

The char yield from chlorogenic acid was enhanced by low heating rates and low temperatures but was independent of the mass of substrate pyrolyzed, at least up to 300 mg. The major components of the gaseous product were catechol, phenol and benzoic acid. The surface area of char increased with temperature to a maximum at 650°C. The oxidative pyrolysis enhanced the surface area but decreased the char yield. The char lost its carbonyl, carboxyl, and aliphatic functionalities completely above 550°C. As a result, the carbonaceous and aromatic character of char increased with temperature and was highest at 750°C.

ACKNOWLEDGEMENTS

The authors are grateful to Philip Morris Management for their support of this research and to Bruce Waymack and Dr. Diane Kellogg for their assistance with mass spectrometer. SEM data were provided by Vicki Baliga.

REFERENCES

1. Sakuma, H., Matsushima, S., Munakta, S., and Sugawara, S. *Agric. Biol. Chem.* 46(5), 1311 (1982).
2. Zane, A. and Wender, S.H. *Tob. Sci.* 7, 21 (1963).
3. Schlotzhauer W.S., Snook, M.E., Chortyk, O.T., and Wilson, R.L. *J. Anal. Appl. Pyrol.* 22, 231 (1992).
4. Fletcher, T.H., Solum, M.S., Grant, D.M., and Pugmir, R.J. *Energy Fuels* 6, 643 (1992).
5. Shafizadeh, F. and Sekiguchi, Y. *Comb. Flame* 55, 171 (1984).
6. Boon, J.P., Pastorova, I., Botto, R.E., and Arisz, P.W. *Biomass Bioenergy* 7, 25 (1994).

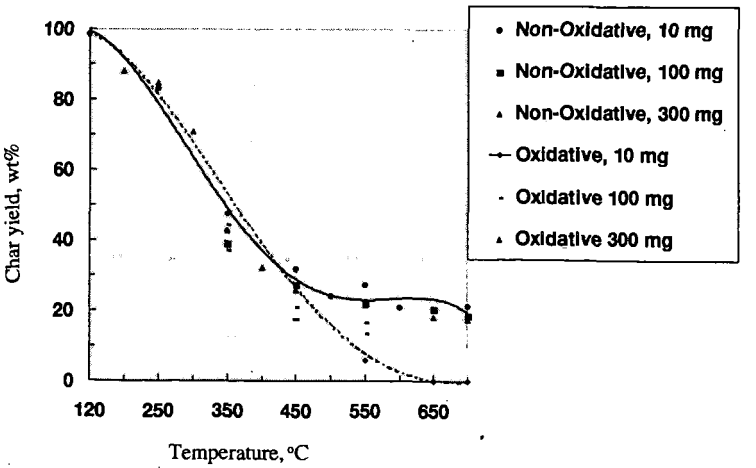

Fig. 1- Effect of temperature on char yield from chlorogenic acid

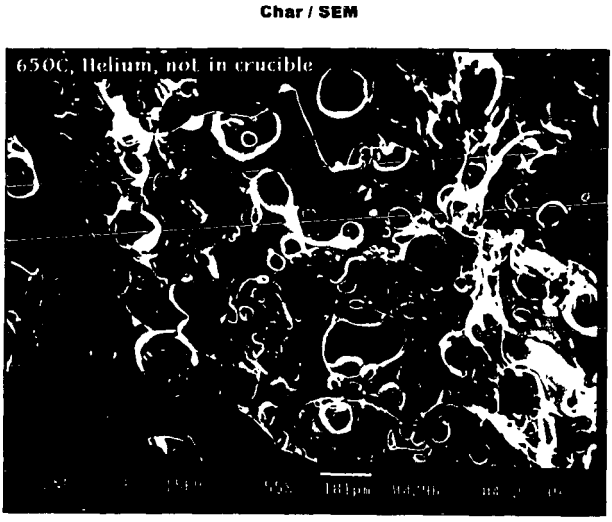

Fig. 2- Surface morphology of the 650°C-char.

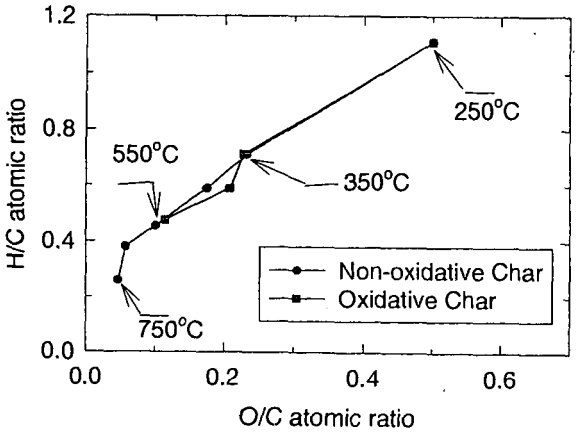

Fig. 3- Relationship between H/C and O/C ratios of chlorogenic acid chars

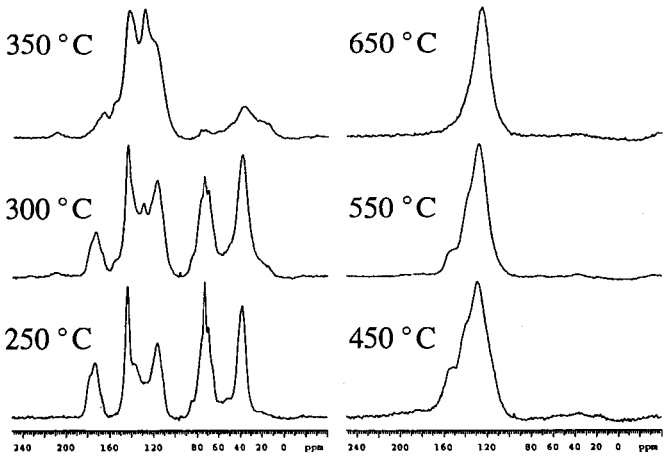

Fig. 4- Solid-state ^{13}C CPMAS NMR spectra of chlorogenic acid chars

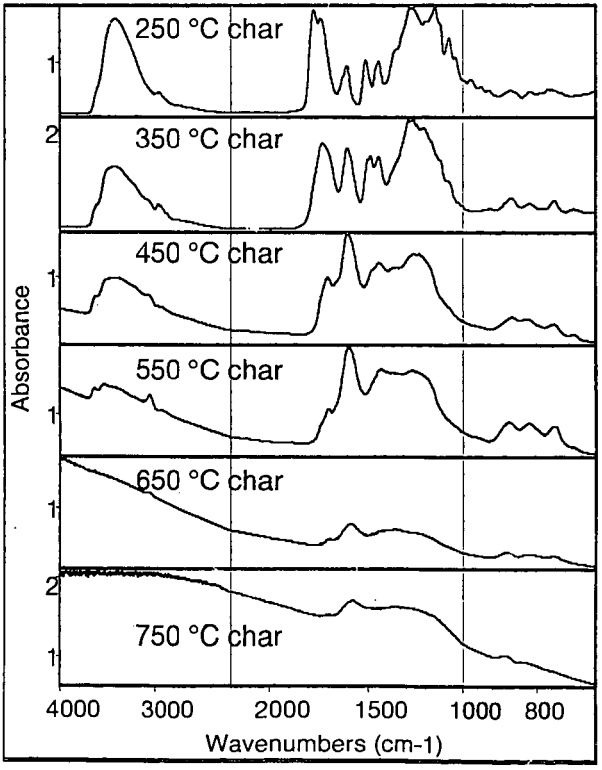

Fig. 5- Fourier-transform infrared (FTIR) spectra of chlorogenic acid chars

EFFECT OF ADDITION OF SALTS ON COAL EXTRACTION IN CS_2/NMP MIXED SOLVENT

Koyo NORINAGA*, Kazuhiro TAKAHASHI, and Masashi IINO
Institute for Chemical Reaction Science, Tohoku University
Katahira, Aoba-ku, Sendai, 980-8577, Japan

KEYWORDS: Coal, Extraction, Salts, CS_2/NMP mixed solvent

ABSTRACT

The effect of addition of various salts on the extraction of seven different kinds of coals with carbon disulfide-*N*-methyl-2-pyrrolidinone (CS_2-NMP) mixed solvent (1:1 by volume) was investigated. Addition of some salts considerably increased the extraction yield for several coals. For Upper Freeport coal, in particular, the addition of a very small amount (0.25 mol/kg-coal) of tetrabutylammoniumfluoride increased the extraction yield from 60 to 84%. The effect of a kind of anions on the extraction yield was also examined. It was found that the charge density of anion is responsible for the increase of the extraction yields. The fractionations of the extracts using pyridine indicate that the extracts obtained with the additive contain heavier constituents than those without the additive.

INTRODUCTION

The extraction of bituminous coals with CS_2/NMP mixed solvent (1:1 by volume) was found to give very high extraction yields at room temperature. [1] It was also observed that the addition of a small amount of electron acceptors such as tetracyanoethylene (TCNE) and 7,7,8,8-Tetracyanoquinodimethane (TCNQ) to the mixed solvent increases the extraction yields significantly. [2,3] For example, the yield of the room temperature extraction of Upper Freeport coal with the 1:1 mixtures of CS_2/NMP increases from 59 to 85 wt% (dry-ash-free basis) by adding only 5 wt% (based on coal) of TCNE to the solvent. [2] The effects of addition of TCNE are reversible. [4] Hence the increase of the extraction yield was found to be not due to the breakage of covalent bonds such as ether bonds in coal but due to the suppression of the association between coal macromolecules via non-covalent bonds. Previous studies on the mechanism for enhancing coal solubility have been concentrated on the charge-transfer complex formation between additives and coal. However the correlation between the solubility of coal and the electron acceptability was rather poor. Furthermore EPR studies of Illinois No.6 coal demonstrate that the increase in the spin concentration by the addition of electron acceptors is not due to the formations of new paramagnetic centers, i.e., thermally accessible triplet state arising from charge-transfer interactions. [5] Thus the formation of the charge transfer complex between the coal and the electron acceptor does not seem to be the plausible mechanism for enhancing coal solubilities. Recently, Chen and Iino proposed another possible explanation for the effect of additives on coal extraction. [6,7] It was found that TCNE does not exist as a neutral molecule in NMP as well as in the NMP/CS_2 mixed solvent but forms TCNE anion derivative, i.e., NMP 1,1,2,,3-pentacyanopropene salt (NPCNP). It has been well known that TCNE easily generate PCNP anion by reacting with aprotic polar solvent such as pyridine [8] or pyridone [9,10] in the presence of the proton source like water. They also examined that the effect of addition of NPCNP on the extraction yields of UF coal with CS_2/NMP mixed solvent. The addition of 0.2 mol/kg-coal NPCNP increases the extraction yield from 59 to 72 wt%, which is comparable to the increment by adding the same amount of TCNE. These observations indicate that the anion plays a key role on the enhancement of the coal solubility. However there is little information available on what kinds of anion is effective for the coal extractions. Furthermore, the effect of additives on the solvent properties such as the Gutmanns donor (DN) and acceptor numbers has not been focused yet.

In the present study, the effect of anion on the coal extraction with CS_2/NMP mixed solvent is examined using tetrabutylanmonium and lithium salts of various anions systematically. The changes in the bulk property of the solvent with adding salts are also examined based on the solvatochromism of well-characterized probe dye indicators. [11,12]

EXPERIMENTAL

Solvent extraction. Seven different kinds of coals were used as coal samples. Their particle sizes were finer than 150 μm. They were dried under vacuum at 353 K for 12 h. The elemental composition of the coal samples are listed in Table 1. 1.0 g of a coal sample was extracted with 60 mL of CS_2/NMP mixed solvent (1:1 by volume) with or without the additive under ultrasonic (38 kHz) irradiation for 30 min at room temperature. The mixtures were subsequently centrifuged under 29000 g for 60 min, and the supernatant was immediately filtered thorough a membrane paper with a pore size of 0.8 μm. The residue was repeatedly extracted with the fresh mixed solvent in the same way, until the filtrate become almost colorless. This exhaustive extraction usually needs the repeating of 4-6 times. The residue was thoroughly washed with acetone to remove CS_2 and NMP retained. Extraction yields

were determined on a dry ash free basis from the amount of the residue. The extract, hereafter referred to as MS was further fractionated using acetone and pyridine to yield acetone soluble (AS), pyridine soluble / acetone insoluble (PS), and pyridine insoluble (PI) fractions, respectively. Detailed extraction and fractionation procedures were described in elsewhere. [1] Several kinds of tetrabutylanmonium and lithium salts were used as additives. Typical amount of the additive was 0.25 mol/kg coal.

Solvatochromism. The effect of addition of LiCl on the DN of NMP was empirically evaluated by using copper(II)-*N*,*N*,*N'*,*N'*-tetramethylethylendiamine-acetylacetonate ($Cu(tmen)(acac)^+$). The probe dye indicator was dissolved in the NMP/LiCl solvent, and the mixture was subjected immediately to the UV/VIS measurements. The DN was calculated using an empirical equation based on the absorption band of the dye in the solvent. [12]

RESULTS AND DISCUSSION

Effects of addition of the salts on the extraction yields of UF coals are shown in Table 2. The extraction yields varies with the types of salts. TBAF affects the coal extraction most significantly and increased the yield up to 84%. The results for the halogenide salts indicate that a kind of halogenide anions affects the extraction yields. The yields increased in the order, $F^->Cl^->Br^->I^-$. This indicates that the anions with the small ion radius or large elecronegativity are effective for the enhancement of the yield. Lewis acidity or basicity of ions can be categorized reasonably by HASB (Hard and Soft Acids and Bases) principle of Pearson. [13] He proposed a simple, useful rule, that is, hard acids bind strongly to hard bases and soft acids bind strongly to soft bases. It is convenient to divide bases into two categories, those that are polarizable (low charge density), or "soft," and those that are nonpolarizable (high charge density), or "hard." F^- and Cl^- are categorized into hard base, while Br^- and I^- are soft base. Hard base tends to attract proton strongly. If we use protic solvents, F^- and Cl^- must be strongly solvated and would show little effect on the extraction. Because the CS_2/NMP mixed solvent is dipolar, aprotic solvent, these anion would be solvated weakly and can interact with some hard acidic sites in coal. Acid - base interaction between coal and anion would be responsible for the enhancement of the extraction yields. On the other hand, soft base such as Br^- and I^- is strongly solvated since the dipolar aprotic solvent such as the mixed solvent can be categorized into soft acid solvent. Hence these soft base can not interact with the coal and have little effect. Non-halogenide anions such as CH_3COO^-, ClO_4^-, and NO_3^- were also used. CH_3COO^- is hard base and increases the extraction yield while others are soft base and the effects are less significant.

Table 3 lists the effect of TBAF addition on the extraction yields of several kinds of coals. Upper Freeport, Lower Kittanning, and Stigler coals are increased their extraction yields with the mixed solvent by the addition of TBAF, but for Pittsburgh No.8, Illinoi No.6 coals the yields did not increase. For the addition of TCNE the same tendency of the extraction yields was obtained for the above-mentioned five coals. The results of the fractionation of MS of Upper Freeport coal are shown in Table 4. The increase in the MS yields is mainly due to the increase of the heaviest extract fraction, i.e., PI, and little increase in the lighter fraction of AS and PS. Figure 1 shows the experimental procedure for examination of the reversibility of the effect of additive on the extraction yields of UF coal. The yield of MS obtained from the extraction with LiCl is 78 wt %. The MS was washed exhaustively with acetone/water mixed solvent (1:4 by volume) to remove LiCl retained, and subsequently extracted with the CS_2-NMP mixed solvent in the absence of LiCl. A portion of MS became again insoluble, i.e., 63 wt % of UF coal is extracted by the mixed solvent. The yield was almost same as the yield of MS obtained without additives. Hence the effects of addition of LiCl seem to be reversible as observed for the addition of TCNE.

Figure 2 shows the effect of LiCl concentration in NMP on the DN of NMP as well as extraction yield with NMP for UF coal. DN of NMP is rapidly increased from 27 to 54 even by the addition of very small amount of LiCl (10 mmol/L) and kept constant value above 10 mmol/L. The extraction yield is also increased by LiCl addition, it increases with increasing the concentration of LiCl up to 120 mmol/L. The increase in the extraction yield is observed even where the DN is almost constant, indicating that the effect of the salt additive on the coal extraction can not be explained only by the change in the bulk property of solvent with salt addition. It is necessary to consider the interaction between coal and anion more in detail.

CONCLUSIONS

The effect of addition of various salts on the extraction of seven different kinds of coals with carbon disulfide-*N*-methyl-2-pyrrolidinone (CS_2-NMP) mixed solvent (1:1 by volume) was investigated. Addition of some salts considerably increased the extraction yield for several coals. For Upper Freeport coal, in particular, the addition of a very small amount, 0.25 mol/kg-coal of tetrabutylammoniumfluoride increased the extraction yield from 60 to 84%. The effect of a kind of anions on the extraction yield was also examined. It was found that the charge density of anion seems to be responsible for the increase in the

extraction yields. The fractionations of the extracts using pyridine indicate that the extracts obtained with the additive contain heavier constituents than those without the additive.

ACKNOWLEDGMENT. This work was supported in part by a "Research for the Future Project" grant from the Japan Society for the Promotion of Science (JSPS), through the 148th Committee on Coal Utilization Technology.

REFERENCES

(1) Iino, M.; Takanohashi, T.; Osuga, H.; Toda, K. *Fuel* **1988**, *67*, 1639.
(2) Liu, H.; Ishizuka, T.; Takanohashi, T.; Iino, M. *Energy Fuels* **1993**, *7*, 1108.
(3) Ishizuka, T.; Takanohashi, T.; Ito, O.; Iino, M. *Fuel* **1993**, *72*, 579.
(4) Iino, M.; Liu, H.; Hosaka, N.; Kurose, H.; Takanohashi, T. *Prepr. Pap. Am. Chem. Soc., Div. Fuel. Chem.* **1997**, *42(1)*, 248.
(5) Thompson, R. T., Rothenberger,K.S.,Retcofsky,H.L. *Energy Fuels* **1997**, *11*, 739.
(6) Chen, C.; Kurose, H.; Iino, M. *Energy Fuels* **1999**, *13*, 1180.
(7) Chen, C.; Iino, M. *Energy Fuels* **1999**, *13*, 1105.
(8) Middleton, W. J.; Little, E. L.; Coffman, D. D.; Engelhardt, V. A. *J. Am. Chem. Soc.* **1958**, *80*, 2795.
(9) Thyagarajan, B. S.; Rajagopalan, K.; Gopalakrishnan, P. V. *Chem. Ind.* **1966**, *5*, 1887.
(10) Thyagarajan, B. S.; Rajagopalan, K.; Gopalakrishnan, P. V. *J. Chem. Soc. (B)* **1968**, 300.
(11) Reichardt, C. *Chem. Rev.* **1994**, *94*, 2319.
(12) Spange, S.; Reuter, A.; Vilsmeier, E.; Heinze, T.; Keutel, D.; Linert, W. *J. Polymer Sci. Part A* **1998**, *36*, 1945.
(13) Pearson, R. G. *J. Am. Chem. Soc.* **1963**, *85*, 3533.

Table 1. Properties of Coal Samples

Coal	Symbol	Ultimate analysis(wt%,daf)				Ash(wt%,db)
		C	H	N	O+S[a]	
Sewell'B'	SW	88.4	5.3	1.4	4.9	4.6
Upper Freeport	UF	86.2	5.1	1.9	6.8	13.1
Lower Kittanning	LK	84.0	5.6	1.7	8.7	9.0
Lewiston Stockton	LS	82.9	5.4	2.0	9.7	19.6
Pittsburgh No.8	PB	82.6	5.5	2.1	9.8	8.7
Stigler	SG	77.8	4.8	1.5	15.9	11.7
Illinois No.6	IL	76.9	5.5	1.9	15.7	15.0

[a] By difference

Table 2. Effect of Salt Types on Extraction Yields [a] of UF Coal

Additive [b]	Extraction yield (wt%,daf)
LiCl	78.1
LiBr [c]	68.7
LiI [d]	60.9
$(n\text{-Bu})_4N^+F^-$	83.9
$(n\text{-Bu})_4N^+Cl^-$	78.8
$(n\text{-Bu})_4N^+Br^-$	61.8
$(n\text{-Bu})_4N^+I^-$	59.3
$(n\text{-Bu})_4N^+OCOCH_3^-$	75.6
$(n\text{-Bu})_4N^+ClO_4^-$	62.1
$(n\text{-Bu})_4N^+NO_3^-$	54.0
None	59.8

[a] CS_2-NMP mixed solvent (1:1 by volume), room temperature
[b] 0.25mol/kg-coal [c] 0.95mol/kg-coal
[d] 1.87mol/kg-coal

Table 3. Effect of TBAF [a] Addition on Extraction Yields [b] of Coals

Coal	C%	Extraction yield (wt%, daf)	
	(dry ash free)	None	0.25mol/kg-coal
SW	88.4	33.9	48.0
UF	86.2	59.8	83.9
LK	84.0	38.0	61.6
LS	82.9	25.6	25.8
PB	82.6	37.8	37.4
SG	77.8	26.0	72.2
IL	76.9	24.6	25.5

[a] $(n\text{-Bu})_4N^+F^-$

[b] CS_2-NMP mixed solvent (1:1 by volume), room temperature

Table 4. Effect of TBAF [a] Addition on Extraction Yields [b] of Coals and Fraction Distributions of the Extracts

Coal	TBAF	Extraction yield (wt%,daf)	Fraction distribution(wt%,daf)		
			AS	PS	PI
UF	None	60.1	8.2	25.0	26.9
	0.25mol/kg-coal	82.4	11.5	12.7	58.2
LK	None	38.7	6.3	27.1	5.3
	0.25mol/kg-coal	63.7	9.4	17.9	36.4
PB	None	43.5	12.3	30.0	1.2
	0.25mol/kg-coal	39.9	11.8	23.4	4.7
SG	None	21.2	6.1	14.5	0.6
	0.25mol/kg-coal	62.4	6.4	17.2	38.8
IL	None	27.9	7.8	19.1	1.0
	0.25mol/kg-coal	27.4	10.0	16.8	0.6

[a] $(n\text{-Bu})_4N^+F^-$

[b] CS_2-NMP mixed solvent(1:1 by volume), room temperature

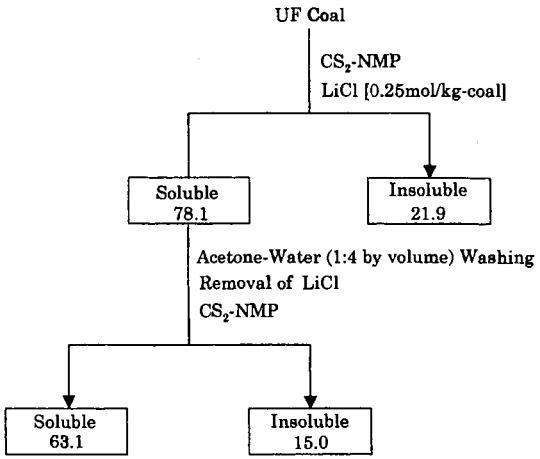

Fig. 1. Reversibility of the Effect of LiCl Addition on the Extraction,Yield

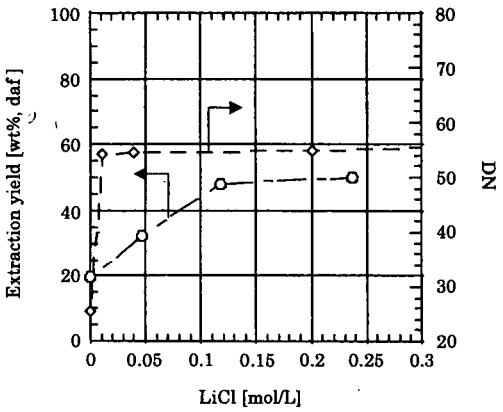

Fig. 2. Effect of LiCl concentration on DN of NMP as well as the Extraction Yield of UF Coal

LOW SEVERITY EXTRACTION OF PITCH FROM COAL AS A PRECURSOR TO VALUE ADDED PRODUCTS - REVISITED.

A.J. Berkovich, C.J. Lafferty and F.J. Derbyshire
Center for Applied Energy Research
University of Kentucky
2540 Research Park Drive, Lexington, KY, USA, 40511.

KEY WORDS: pitch extraction, fibres, anthracene oil.

ABSRACT: This paper presents preliminary results from a detailed investigation into different methods of extraction of pitch from coal and their affect on the properties of the final pitch product. One such method is the use of cheap and readily available petroleum residues that act as solvents for pitch. Crude anthracene oil, a cheap petroleum residue was shown to extract a reasonable yield of high boiling point material from coal at low temperatures with no over pressure. A series of extractions at temperatures ranging from 200 to 450 °C were performed on coals differing in rank and heteroatom contents. The results indicate that maximum extraction yield occurs between 350 and 400 °C. The extraction capability of recycled anthracene oils recovered from prior extractions was also assessed. Carbon fibres from pitch extracts were produced and their physical properties assessed.

INTRODUCTION: The use of coal derived pitches as precursors for valued added carbon products is well known. As the range of applications for new carbon based products increases the potential exists to tailor precursor properties for specific applications, for example carbon fibres. This paper examines pitch extraction methods and how different extraction conditions effect the properties and performance of pitch derived carbon fibres as a lead into tailoring properties of extracted pitches.

Petroleum residues, such as anthracene oil and petroleum based solvents have been shown to be good solvents for high boiling point liquids from coal (coal derived pitches) [1-4]. However, previous work on coal solvent extraction using such solvents has usually involved pre-hydrogenation of the solvent as well as high gas over pressures during the extraction. Hydrogenation and high pressure extractions adversely affect the economic potential of a solvent extraction process. The aim of this paper was to prepare pitches using mild extraction conditions and assess the potential of these pitches as precursors to value added carbon products.

EXPERIMENTAL: Pitch extractions were performed in 50 mL stainless steel tubing bomb reactors which were heated in a fluidised sand bath while being shaken by a mechanical shaker. Coal samples were crushed to < 60 mesh and then slurried in different ratios with the solvent before being placed into the tubing bombs. Two different solvents were used, anthracene oil as well as panasol (a commercially available petroleum derived solvent). The solvents were not hydrogenated nor was any gas over pressure used during the extractions. Extraction temperatures ranged from 250 to 450 °C, with extraction between 10 minutes and 3 hours. After extraction, the reaction mixture was extracted in a Soxhlet apparatus using THF. The THF soluble fraction was then vacuum distilled to 300 °C at 1 mm Hg. The THF insoluble residue was dried in a vacuum oven and its mass used to calculate the yield of extracted material. The softening point of the extraction pitch material was measured. Typically a softening point of 200 to 240 °C was desired for ease of fiber forming and processing. The fiber forming and processing methods have been described elsewhere [5]. Coal samples from Northeast Wyoming's Black Thunder mine and Western Kentucky was used for the extraction experiments. Proximate analyses of the coals showed, Black Thunder contained: 8.89 % moisture; 5.76 % ash; 39.88 % volatile matter; 45.47 % fixed carbon, the Western Kentucky contained: 2.30 % moisture; 8.90 % ash; 34.42 % volatile matter; 53.45 % fixed carbon.

RESULTS and DISCUSSION: Mild condition solvent extractions were preformed on Black Thunder coal. The effect of temperature was examined first. Extractions with coal to solvent ratios of 1:2 with anthracene oil and panasol were performed at 200, 250, 300, 350, 400 and 450 °C for 1 hour. Figure 1 compares the effect of temperature on extraction yield for Black Thunder coal using anthracene oil and panasol. Figure 1 shows that anthracene oil produced a higher yield of pitch compared to panasol with the maximum extraction yield occurring at approximately 350 °C for anthracene oil and approximately 450 °C for panasol.
The effect of different extraction time was also examined. Again a coal to solvent ratio of 1:2 was used and extraction times of 10 minutes to 3 hours were examined. Figure 2 shows extraction yield versus extraction time. Inspection of Figure 2 shows that 80 % of the extraction yield is attained during the first 20 minutes.

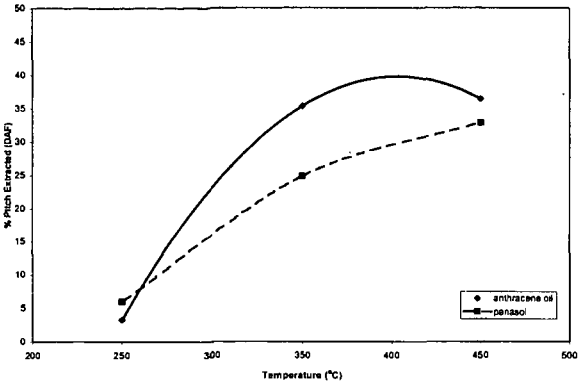

Figure 1 – Effect of temperature on extraction yield for Black Thunder coal.

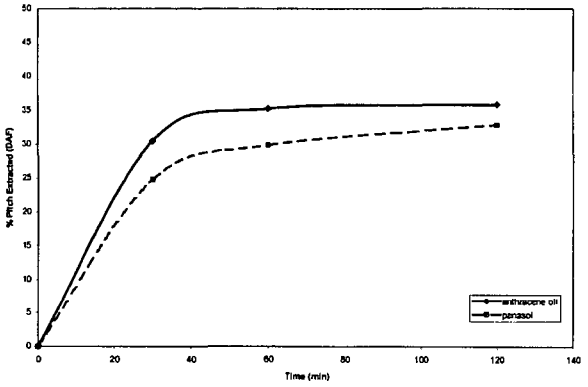

Figure 2 – Effect of time on extraction yield for Black Thunder coal.

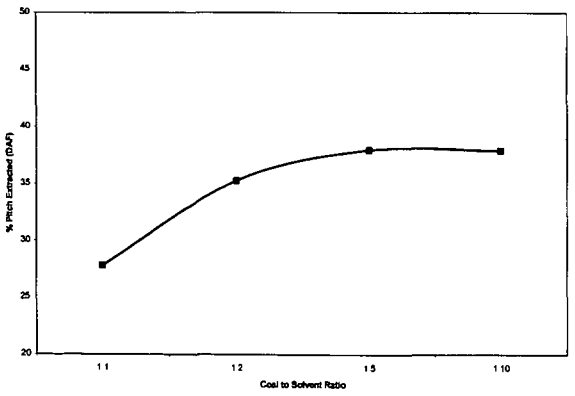

Figure 3 – Effect of increasing solvent concentration on extracted pitch yield

The effect of coal to solvent ratio was also examined, Figure 3 shows a plot of extracted pitch yield versus solvent to coal ratio where anthracene oil was used. Figure 3 shows that using coal to solvent ratios greater than 1:2 did significantly increase the pitch yield. From the results of these preliminary experiments the following extraction parameters were used for subsequent extractions: coal to solvent ratios of 1:2; extraction temperature, 350 °C; extraction time, 60 minutes. The re-use of solvent recovered from distillation was also investigated. Pitch

extractions were preformed on Black Thunder coal using recycled solvent as well as mixtures of recycled and fresh solvent. Table 1 shows extracted pitch yields for these experiments. The results showed only a slight decrease in extraction yield for the recycled solvents compared to fresh solvent. The mixtures of fresh and recycled showed almost the same extraction capabilities as the fresh solvent.

Table 1 - Extracted pitch yields for recycled solvents, yields for fresh solvent shown in brackets.

Solvent	% Yield
recycled anthracene oil	28.3 (35.3)
recycled panasol	20.0 (24.82)
1:1 recycled anthracene oil and fresh anthracene oil	35.2
1:1 recycled panasol and fresh panasol	26.8

A summary of pitch extraction conditions and yields is shown on Table 2. The results show that extractions preformed on Black Thunder coal under mild conditions have lower extracted pitch yields compared to those using more severe conditions. Tables 2 and 3 contain characterisation data for the extracted pitches. The results show that pitches extracted under mild conditions have very similar characteristics to those extracted under severe conditions. More importantly however, are the characteristics of the fibres formed from the extracted pitches.

Table 2 – Summary of extraction yields and extraction methods.

Coal	Extraction Method	% Yield	Extracted Pitch
Black Thunder	a.oil; 350; 60	35.3	BT1
Western Kentucky	a.oil; 350; 60	90.6	WK1
Black Thunder	pan; 350; 60	24.8	BT2
Western Kentucky	pan; 350; 60	89.2	WK2
Black Thunder	a.oil; 370; 60; H_2	90.0	BT3

Extraction Method: solvent; temperature (°C); time (min)
a.oil = anthracene oil, pan = panasol

Table 3 – Summary of extracted pitch properties.

Pitch	Softening Point (°C)	Ultimate Analysis (% DAF)				
		C	H	N	O	S
BT1	220	87.6	5.03	1.1	1.6	0.5
WK1	210	91.1	4.5	1.7	1.7	1.0
BT2	220	85.7	5.8	1.4	6.8	0.3
WK2	260	90.2	4.3	1.8	2.5	1.1
BT3	230	87.1	6.0	1.4	5.2	0.3

Carbon fibres formed from the extracted pitches were tested for strength, modulus and resistivity. A summary of these properties is shown in Table 3. Table 3 shows that the physical properties of the carbon fibres formed from pitches extracted under severe and mild conditions are similar.

Table 3 – Summary of properties of pitch derived carbon fibers.

Extracted Pitch	Strength (MPa)	Modulus (GPa)	Resistivity $m\Omega cm^{-1}$
BT1	400	82	8.0
WK1	576	86	47
BT2	319	63	16.7
WK2	347	69	16.3
BT3	380	n/a	27.3

The results show that although extraction yields are lower for the mild condition extractions compared to the severe condition extractions, the properties of the extracted pitches and pitch based fibres are similar. Therefore there is the potential to produce pitch from coal using a low

temperature and low pressure method without sacrificing the performance of the final carbon product.

CONCLUSIONS: Low severity solvent extraction of coal using anthracene oil and panasol were performed to produce a high boiling point liquid, pitch. The pitch extraction yields of the mild condition techniques were compared to those performed under more severe conditions. Although the low severity extractions showed lower yields the chemical characteristics of the extracted pitches were similar to those extracted under more severe conditions. The physical characteristics of carbon fibres formed from pitches extracted under mild and severe conditions were similar.

REFERENCES

1. Oele, A.P., Waterman, H.I., Goedkoop, M.L. and van Krevelen, D.W. *Fuel*, **1951**, *30*, 169.
2. Mishra, S. and Sharma, D. K. *Fuel*, **1990**, *69*, 1377.
3. Rosal, R., Diez, F.V. and Sastre, H. *Ind. Eng. Chem. Res.*, *1992*, **31**, 2407.
4. Cloke, M. and Wang, C. *Energy & Fuels*, **1995**, *9*, 560.
5. Jorro, M. and Ladner, W.R. 4th Int Carbon Con, London, Sept 1974.

CHANGE IN THE PORE SIZE DISTRIBUTION OF BROWN COAL ALONG WITH A PROGRESS OF MOISTURE RELEASE

Haruo Kumagai[1] and Kazuo Nakamura[2]
[1]Center for Advanced Research of Energy Technology, Hokkaido University,
Kita-13, Nishi-8, Kita-ku, Sapporo 060-8628, Japan
[2]Research and Development Department, Osaka Gas Co., Ltd.,
6-19-9, Torishima, Konohana-ku, Osaka 554-0051, Japan

Keywords : pore, moisture release, macromolecular structure, CAMD

INTRODUCTION

Molecular modeling technique has been employed widely in biological chemistry to provide insight into the conformation, properties and interactions of biomolecules. According to existing development of molecular modeling software, the methodology has allowed treatment of relatively large molecules and has begun to be applied to fuel chemistry by constructing complex heterogeneous macromolecular model. Carlson [1] applied computer-aided molecular design (CAMD) methods to determine three-dimensional minimum-energy conformations for four bituminous coal models. He indicated that nonbonding interactions, in particular, van der Waals and hydrogen bonding interactions, are strong driving forces to form and stabilize the structures of the coal models. Takanohashi and co-workers also determined the minimum-energy conformation of a bituminous coal by a CAMD method and suggested that the coal has a possibility to have an associated structure of constituent molecules in the coal having a continuous distribution of molecular weights [2,3].

Low rank coals such as lignite and brown coal are featured by their high residual moisture contents in the range from 30 to 70wt%. Because of such a high moisture content, moisture removal is the primary and essential step in almost all brown coal utilization processes. Furthermore, the drying step is known to have a significant effect on the physical and chemical characteristics of the dried coal. For example, it has been suggested that drying have negative impact on liquefaction reactivity [4-7] and that in lignite liquefaction the oil yield is higher for dried coal than that for raw or partly dried one [8]. These nominal impacts of drying on the conversion reactivity can be attributed to an irreversible change of pore structure that results in a limitation of accessibility of reacting components [9]. And it is easy to imagine that the pore structure change is brought about by the change in macromolecular structure of coal along with drying.

In a previous paper [10], we investigated the change in conformation for an Australian brown coal with its moisture removal process by means of a CAMD method. The results indicated that change in conformation of the coal simulated by CAMD method is well corresponding to the observed volumetric change, and removal of water molecules results in a drastic conformational change in the final stage of moisture removal. In the present study, conformations of an Australian brown coal are simulated under 3D periodic boundary conditions in order to elucidate the change in the pore distribution along with a progress of moisture release.

CAMD calculation method

The CAMD study was carried out by using an O_2 workstation (Silicon Graphics, Inc.) with Cerius^2 software (version 3.8, Molecular Simulations Inc.). The software is capable of calculating the most stable structures with the minimum conformational energies using COMPASS, UNIVERSAL and DREIDING force fields. Since our previous study indicated the importance of hydrogen bonding interactions on the stabilization of brown coal conformation,

the DREIDING 2.21 force field was used in this study. Cerius[2] software allows the use of periodic boundary condition, in which model molecules are placed in a unit cell surrounded by the same cells in all directions. Molecular segments in the cell can interact with others in the neighboring cells as well as in the same cell. If a segment exits on the one surface of the cell, the same one enters from opposite side. The structure of Australian brown coal (Yalloum brown coal ; YL) was modeled by two oligomers, namely a pentamer (Mw=1892) and an octamer (Mw=3074), of unit structure. The unit structure, which was constructed on the basis of the data from elemental analysis and 13C-NMR spectroscopy of the coal [11], is shown in figure 1. Each oligomer was specially arranged so as to have no interaction with others. Simulations of moisture removal process were initiated by generating 413 water molecules (59.95wt%, wet basis) surrounding the model molecule and the **minimum energy conformation** (**MEC**) for the model with water molecules was calculated based on molecular mechanics and molecular dynamics methods. After **MEC** was obtained, the volume and density of unit cell and pore distribution were calculated. The pore volume was defined as prove occupiable volume using several size of spherical probe in radius from 0.5Å to 3.0Å. The calculation was repeated decreasing the number of water molecules step by step to 0, and finally **MEC** for model molecule with 0 water, i.e., completely dried coal was obtained.

RESULTS AND DISCUSSIONS

Change in the volume and in the density of **MEC** unit cell which contain model molecules of YL and water molecules are shown in figure 2 as a function of the extent of moisture removal (%). During moisture release process, the volume decreases monotonously with moisture removal, and reaches nearly a half of initial volume. Initial density of the cell (1.110 g/cm^3) is in a good agreement with experimentally determined raw coal density [12, 13], while density of the cell for completely dried YL (0.929 g/cm^3) is slightly higher than mercury density of dried YL (0.873 g/cm^3). As shown in figure 2, density of the cell decreases gradually with the extent of moisture removal up to 80%. A significant decrease in density of the cell is observed with the extents higher than 80%. In the previous study [10], we demonstrated that change in the volume for YL model molecules without water molecules proceeds in the final stage of moisture removal at which non-freezable water is removed, and the change in volume corresponds well to the change of non-bonding interaction energies. The significant decrease in density observed in this study is well in harmony with the previous study. Thus, the result indicates that the dense conformation of YL model molecules with water molecules changed to porous one with removal of non-freezable water.

Micropore size distribution is calculated from occupiable volume with spherical probe, Vocc, and radius of the prove, Rp. The micropore size distribution curves, dVocc/dRp vs Rp, are shown in figure 3. The micropore size distribution is little affected with extent of moisture removal at the range from 0% to 65%. As we can expected from change in the cell density, described above, a significant change in the distribution is observed with the extents higher than 80%. The change in micropore size distribution shows the enlargement in pore size that has occurred at the final stage of moisture removal. The total micropore volume increases from 0.15 cm^3/g for wet YL (0% moisture removal) to 0.30 cm^3/g for completely dried coal, down to a micropore size of 0.5Å. The change corresponded well to the change of density.

Although techniques are available for the characterization of the micropore structure of dried coal, there are no equivalent procedures to determine the micropore structure of coal in a wet state. Setek and co-workers [14] have applied small angle X-ray scattering (SAXS), and CO_2 sorption technique to determine the microporosity of YL. The micropore volumes for dried YL show reasonable agreement by the two techniques (0.058 cm^3/g for CO_2 sorption, 0.060 cm^3/g for SAXS) and slightly larger than comparable micropore volume (Rp>2.75Å) obtained by CAMD (0.032 cm^3/g). The micropore volume for wet YL obtained by SAXS (0.110 cm^3/g) is much

larger than that calculated by CAMD (0.001 cm^3/g). This probably reflects differences in the size of the structures to determine the microporosity of brown coal.

In summary, the change in volume and density for YL model molecule with its moisture release process could be successfully simulated by using the CAMD method. Although the coal model molecule employed in this study is rather simple and small, the results appear to represent the characteristics of the brown coal, at least change in the density and micropore size distribution along with a progress of moisture release.

REFERENCE

1. Carlson,G.A. Energy Fuels 1992, 6, 771.
2. Takanohashi,T.; Iino,M.; Nakamura,K. Energy Fuels 1994, 8, 395.
3. Nakamura,K.; Takanohashi,T.; Iino,M.; Kumagai,H.; Sato,M.; Yokoyama,S.; Sanada,Y. Energy Fuels 1995, 9, 1003.
4. Gorbaty,M.L. Fuel 1978, 57, 796.
5. Atherton,L.E. Proc. Int. Conf. Coal Sci. 1985, 553.
6. Neavel,R. Fuel 1976, 55, 237.
7. Cronauer,D.C.; Ruberto,R.G.; Silver,R.S.; Jenkins,R.G.; Davis,A.; Hoover,D.S. Fuel 1984, 63, 77.
8. Vorres,K.S.; Wertz,D.L.; Malhotra,V.; Dang,Y.; Joseph,J.T.; Fisher,R. Fuel 1992, 71, 1047.
9. Vorres,K.S.; Kolman,R.; Griswold,T. Prepr. Pap. Am. Chem. Soc., Div. Fuel Chem. 1988, 33 (2), 333.
10. Kumagai,H.; Chiba,T.; Nakamura,K. Prepr. Pap. Am. Chem. Soc., Div. Fuel Chem. 1999,
11. Yoshida,T.; Narita,Y.; Yoshida,R.; Ueda,S.; Kanda,N.; Maekawa,Y. Fuel 1982, 61, 824
12. Higgins,R.S.; Kiss,L.T.; Alladice,D.J.; George,A.M.; King,T.N.W. SECV Research and Developmemt Department Report No. SC/80/17
13. Higgins,R.S.; Kiss,L.T.; George,A.M.; King,T.N.W.; Stacy,W.O. SECV Research and Developmemt Department Report No. SC/81/28
14. Setek,M.; Wagerfeld,H.K.; Stacy,W.O.; Kiss,L.T. Fuel 1983, 62, 480

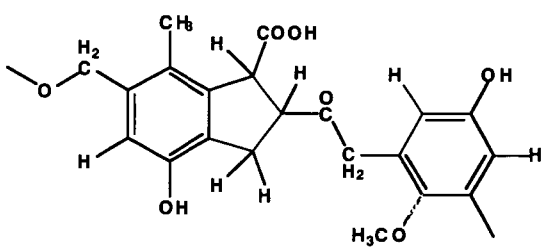

C:65.6, H:5.2, O:29.2 wt%
Mw:384.37
H-bond acceptor:7, H-bond donor:3

Figure 1. Unit structure assumed for YL model molecule.

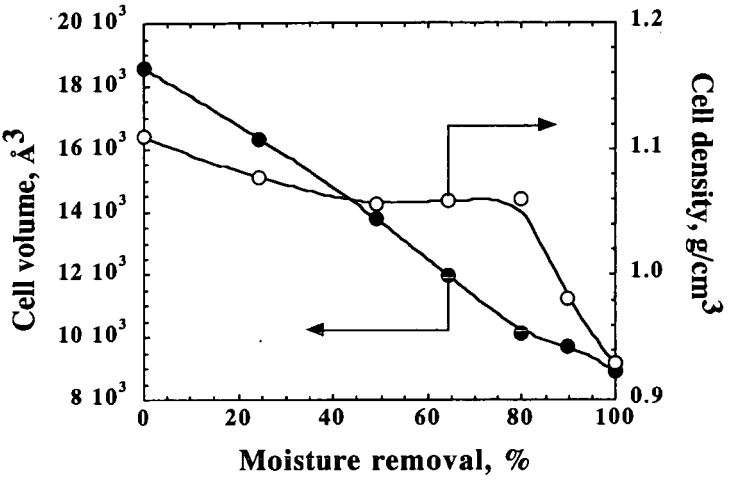

Figure 2. Change in the cell volume and density with extent of moisture removal.

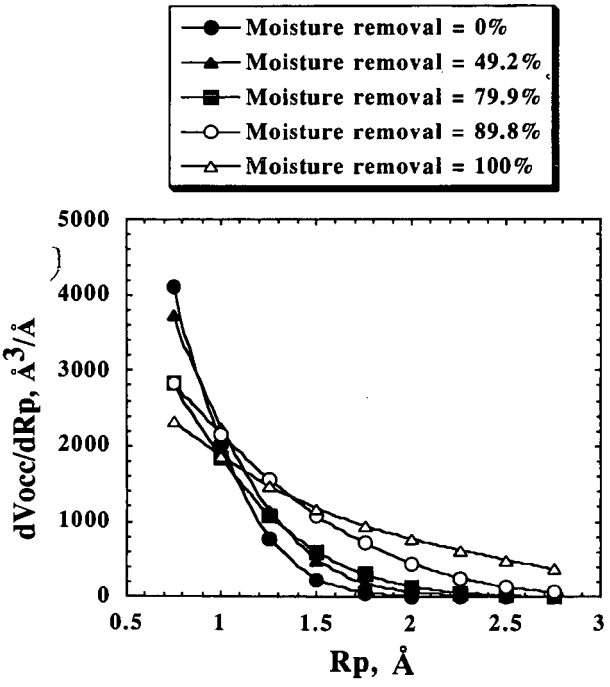

Figure 3. Micropore size distribution curves.

CLUSTER GEOMETRY OF SUPERCRITICAL Xe CONFINED IN CARBON MICROPORES.

M. Aoshima, T. Suzuki, and K. Kaneko

Materials Science, Graduate School of Science and Technology, Chiba University

Yayoi 1-33, Inage, Chiba, 263-8522 Japan

KEYWORDS: Xe adsorption, Cluster structure, Activated carbon

INTRODUCTION

Recently various kinds of porous carbon materials have been developed and their properties and structures have been gathering great concerns in science. There are two types of pores of intraparticle pores and interparticle ones[1]. The carbon nanotube of which pore wall is composed of graphitic sheets has crystalline intraparticle pores[2], when their caps are removed. Activated carbons of the most popular adsorbents are obtained by the activation reaction of carbon materials using H_2O or CO_2. Activated carbon has ill-crystalline intraparticle pores. As activated carbon has excellent adsorptive properties, fine characterization of the pore structure and control of the adsorptive property have been strongly desired. Activated carbon of fiber morphology, so called activated carbon fiber ACF[3], is one of hopeful carbon materials. This ACF has considerably uniform slit-shaped micropores without mesopores, showing excellent adsorption properties. The pore size distribution of ACF is very narrow compared with that of traditional granular activated carbon. Consequently, we can understand more an unresolved problem such as adsorption of supercritical gas using ACF as an microporous carbon.

There are many important supercritical gases such as O_2, N_2, CH_4, NO, and H_2 which are deeply associated with energy, environmental, food, and medical technologies. Further understanding of supercritical gas adsorption is requested to support important technologies. Although vapor adsorption on micropores, which is called micropore filling, is considerably understood, micropore filling of a supercritical gas has not been studied sufficiently irrespective of its importance in micropores[4-7]. We need more fundamental understanding of supercritical gas adsorption. The critical and boiling temperatures of the Xe gas are 289.6K and 165.9K, respectively. The size of a spherical Xe molecule is 0.396nm and the Xe-Xe interaction energy is 217K[8,9]. Accordingly a considerable amount of Xe can be adsorbed in micropores above the critical temperature only by the dispersion interaction. Xe gas has a potential for important applications such as anesthetic and Xe lamp.

In this work, the relationship between micropore filling of supercritical Xe in micropores of ACF at 300 K and cluster size distribution by cluster analysis is described.[10,11]

EXPERIMENTAL

Pitch-based ACFs (P5, P10, and P20) were used. The micropore structures of ACFs were determined by the N_2 adsorption isotherm at 77K using the gravimetric method after the pre-evacuation of ACF samples at 383K. The N_2 adsorption isotherm was analyzed by use of the

in Table 1. The average pore width of these ACFs is in the range of 0.75 to 1.05 nm, corresponding to the model graphite pore.

All adsorption isotherms of supercritical Xe at 300K were onvex in the low pressure range, which can be approximated by the Langmuir equation. In particular, the adsorption isotherm of Xe on P5 having the smallest pores was of

Table 1. Micropore parameters of pitch-based ACF samples

	Surface Area m^2g^{-1}	Micropore Volume mlg^{-1}	Pore Width nm
P5	900	0.336	0.75
P10	1435	0.614	0.86
P20	2190	1.136	1.05

the representative Langmuir type. The smaller the pore width, the greater the amount of Xe adsorption in the low pressure region. The absolute amount of Xe adsorption was very great even at 60kPa, being larger than 250 mgg^{-1} regardless of the supercritical conditions. The fractional filling values of Xe adsorption at 60 kPa for P5, P10, and P20 were 0.29, 0.14, and 0.09, respectively. Here, the volume occupied by Xe was calculated by use of the bulk liquid density (3.06 gml^{-1} at 159 K). Then, these ACFs have enough strong molecular field for Xe to be adsorbed even above the critical temperature. In such a case, the DR equation for vapor must be extended to the adsorption of supercritical gas.

Simulated Xe adsorption isotherms

The adsorption isotherms of Xe in the graphite slit pore of w = 0.90 to 1.00 nm at 300 K were simulated using the GCMC method. Both simulated isotherms increase with the Xe pressure and bend upward above 50kPa. In particular, the adsorption isotherm of w = 0.90 nm had steeper uptake near 50kPa than that of w = 1.00 nm. The upward bending suggests a strong Xe-Xe interaction, accompanying with the cluster formation. Although the simulated isotherms did not agree with experimental one, both results indicate the possibility of the cluster formation upon filling of Xe in the micropore. If there is the cluster formation upon filling in the real ACF system, the further adsorption is blocked near the entrance of slightly wedge-shaped micropores due to the cluster formation; the adsorption isotherm should become Langmurian, as observed.

Xe Cluster size distribution and geometrical cluster structures

We analyzed the snapshots obtained from the GCMC simulation at different pressures for w = 0.90 nm system. The cluster analysis evidenced the presence of clusters in the snapshots, giving the cluster size distribution. Before the rising of the isotherm (at 33.7 kPa), 62% of adsorbed Xe molecules are monomers, but we can find 27% of the dimers there; at 50.5 kPa, the percentage of Xe dimers is 30% and even 16% of the trimers are formed. Just after the steep rising at 75.5 kPa, there is the wide distribution of the cluster size; the molecular number in the cluster is in the range up to 12. At 113 kPa the percentage of the monomer drops to 23%, because small Xe clusters merge into greater clusters. Therefore, even above the critical temperature in micropores Xe molecules are associated with each other to form great clusters which can be a precondensed state. This fact supports the idea that predominant adsorption of supercritical gas needs the stable cluster formation between adsorbate molecules.

subtracting pore effect (SPE) method for the α_s-plot with the reference of the standard N_2 adsorption isotherm of nonporous carbon black[3,12]. The high purify Xe gas was adsorbed on ACF samples at 300K after pre-evacuation of ACF samples at 383K and 1mPa for 2 h. The Xe adsorption isotherm at 300 K was also measured gravimetrically.

GCMC SIMULATION AND CLUSTER ANALYSIS

The established grand canonical Monte Carlo simulation procedure was used. The random movement of molecules makes new configurations and they are accepted according to Metropolis's sampling scheme[13,14]. The pressure P for a chemical potential was directly calculated from the molecular density using GCMC simulation without the wall potential. The radial distribution function (RDF) was calculated. The intensity of RDF at a distance r was obtained from the average number of molecules which are coordinated at the distance between r and r+Δr (Δr = 0.01nm) for all Xe molecules in 1000 snapshots of the equilibrium state. It was divided by $2\pi r$, because we analyzed only monolayer adsorption region. We used the 12-6 Lennard-Jones potential for the fluid-fluid interaction. The Lennard-Jones parameters of ε_{ff}/k = 276.17K and σ_{ff} = 0.396nm[8,15] were used. The interaction potential of a Xe molecule with a single graphite slab was approximated by Steele's 10-4-3 potential function[16]. The fitted parameters of the Xe-carbon potential well depth and effective diameter (σ_{sf}) were obtained with the use of the Lorentz-Berthelot rules.

We used an established technique of the slit-shaped unit cell in x and y directions[17,19]. The size of the rectangular cell was $l \times l \times w$, where l and w are the unit cell length and slit width, respectively. The rectangular box is replicated two-dimensionally to form an infinite slit shaped micropore. Here, the w is not equal to the physical width of H, which is defined as the distance between opposite carbon atom layers, but w is the empirical slit width which is the pore width from the molecular adsorption experiment. The w is associated with H by eq. 1[20].

$$w = H - (2z_0 - \sigma_{ff}), \quad z_0 = 0.856\sigma_{sf} \tag{1}$$

where z_0 is the distance of closest approach. In this work, only model graphite model pore of w = 0.90 was calculated.

In the cluster analysis, local molecular configurations of low energy in the equilibrium are presumed to be clusters. The cluster distribution is obtained using the equilibrium snapshots, when the following function $F(\{n_j\})$ is a minimum. We calculated $F(\{n_j\})$ and determined the cluster distribution using the Metropolis method.

$$F(\{n_i\}) = U(\{n_i\}) - TS(n_i\}), \quad U(\{n_i\}) = \sum_j U_j, \quad S(\{n_i\}) = k(\ln N! - \sum_j \ln n_j!) \tag{2}$$

Here the number of molecules in the ith cluster is n_i, the total number of molecules N, and the number of ways of allocating N molecules to a given partition $\{n_i\}$. U_j is the cluster formation energy of the cluster j, which consists of n_j molecules; U_j is the sum of each intermolecular potential. $S(\{n_i\})$ is the allocation entropy of partition[21].

RESULTS AND DISCUSSION

Microporosity and adsorption isotherms of supercritical Xe

The adsorption isotherms of N_2 at 77K on three kinds of ACFs were of Type I, indicating the presence of uniform micropores. The N_2 adsorption isotherm was analyzed by the α_s-plot with the subtracting pore effect (SPE) method[12]. Both α_s-plots gave an predominant upward deviation below α_s=0.5 due to the enhanced adsorption. The micropore parameters from these α_s-plots for the N_2 adsorption isotherms were determined by use of the SPE method, as given

The intra-cluster radial distribution RDF at 75.5 kPa was calculated. It had a very short peak at 0.44nm corresponding to the dimer at 33.7kPa for both pores. The peak at 0.44 nm indicates the presence of dimers and trimers of regular triangle shape. Also a week peak at 0.76 nm was observed, suggesting the presence of the complex structure of the regular triangles. Thus, Xe molecules form more and greater clusters having the complex geometrical structure are formed in narrower pores under supercritical conditions.

Acknowledgment

This work was funded by the NEDO project from Japanese Government.

References

1. K. Kaneko, J. Membrane Sci., **96** (1994) 59.
2. S. Iijima, Helical microtubes of graphitic carbon, Nature, **354** (1991) 56.
3. Kaneko,C. Ishii, N. Nagai, Y. Hanzawa, N. Setoyama, and T. Suzuki, Advances Colloid Sci.**76-77** (1998) 295.
4. K. Kaneko, and Murata, K., Adsorption, **3** (1997) 197.
5. K. Kaneko, Langmuir, **3**(1987)357.
6. K.Kaneko, Colloid Surf., 37 (1989)115.
7. Z.M.Wang, , T.Suzuki, , N.Uekawa, K.Asakura, and K.Kaneko, J. Phys. Chem., **96** (1992)10917.
8. J.O.Hirschfelder, C.F.Curtiss, R.B.Bird, Molecular Theory of Gases and Liquids, Wiley, New York, 1954.
9. A. J.Stone, The Theory of Intermolecular Forces, Clarendon press. Oxford, 1996.
10. M. Aoshima, T. Suzuki, and K. Kaneko, Chem. Phys. Lett.**310**(1999) 1.
11. M. Aoshima, K. Fukazawa, and K. Kaneko, J. Colloid Inteface Sci. in press.
12. N. Setoyama, T. Suzuki, and K.Kaneko, Carbon, 36(1998) 1459.
13. N. Metropolis, A. W. Rosenbluth, M. N. Rosenbluth, A. H. Teller, J. Chem. Phys. **21** (1953) 1084.
14. M. P. Allen, D. J. Tildesley, Computer Simulation of Liquids, Oxford University Press, Oxford, 1987
15. A. J. Marks, J. N. Murrell, A. J. Stace, J. Chem. Soc. Faraday. trans., **87** (1991) 831.
16. W. A. Steele, Surf. Sci., **36** (1973) 317.
17. K. E. Gubbins, Molecular Simulation, **2** (1989) 223.
18. R. F. Cracknell, D. Nicholson, N. Quirke, Mol. Phys., **80** (1993) 885.
19. T. Suzuki, K. Kaneko, K. E. Gubbins, Langmuir, **13** (1997) 2545.
20. K. Kaneko, R. F. Cracknell, D. Nicholson, Langmuir, **10** (1994) 4606.
21. G. N.Coverdale, R. W.Chantrell, G. A. R.Martin, A.Bradbury, A.Hart, and D. A.Parker, J. Magnet. Magnet. Matter., **188** (1988) 41.

LASER-INDUCED INTERACTION OF SILICA WITH METHANE

V. M. Marchenko †, D. I. Murin †, and S. V. Lavrishchev ‡
† General Physics Institute of the Russian Academy of Sciences,
38 Vavilov Street, Moscow 117942, Russia;
tel.: +7 (095) 135 3437, facsimile: +7 (095) 135 0270,
e-mail: vmarch@kapella.gpi.ru
‡ Laser Materials and Technology Research Center of GPI of RAS,
tel.: +7 (095) 132 8393, e-mail: lavr@lst.gpi.ru

KEYWORDS: Silica reduction, laser thermochemistry.

INTRODUCTION

Laser distillation technique advanced by investigations of energy balance in a laser plume formed on the surface of silica (SiO_2) under the action of radiation of the 10.6 mm wavelength was proposed in [1]. The small depth of absorption (≤20 μm) and the low thermal conductivity resulted in surface heating of silica glass, accompanied by sublimation at $T_s > 1.8$ kK. A continuous laser plume appeared at the laser radiation intensities 1 - 6 kW/cm^2 when the target surface was heated to a temperature exceeding the boiling point $T_b \approx 3$ kK [2,3] and the saturated vapor pressure above the surface rose above the atmospheric value. At this laser radiation power the rate of loss of the target material by sublimation of ~3 mg/s and the specific laser radiation energy of evaporation of silica glass was of 30 kJ/g. A continuous laser plume at the tip of a silica glass rod in air represented a gasdynamic jet of the products of sublimation of SiO_2 at temperatures $T \geq T_b$ escaping into the surrounding atmosphere. According to thermo-chemical analyses [3] at the boiling point T_b thermal decomposition of SiO_2 occurs and composition of the saturated vapor above SiO_2 is governed by equilibrium chemical reaction $SiO_2 \rightarrow 57.6\ SiO + 6.6\ O + 25.8\ O_2 + 10.0\ SiO_2$. Cooling of the gaseous products of sublimation by the emission of thermal radiation and by heat exchange with the ambient gas resulted in chemical recombination of these products and condensation of SiO_2 in submicron particles. Deposition of particles on substrates during continuous laser distillation of SiO_2 resulted in synthesis of bulk samples of porous and vitreous structure varied with the temperature of substrates. Laser distillation is useful for rapid synthesis of high-purity and doped samples of silica materials with variable optical properties, including silica nanocomposites [4]. Fluorine-doped silica glasses were synthesized by initiating chemical reactions of the products of pyrolysis in a laser plume with a gas containing freon [5].

Chemical reduction of silica SiO_2 with carbon, hydrogen, and hydrocarbons occurs at high temperatures [6]. Initial stage of the synthesis of Si crystals is smelting of metallurgical silicon in electric furnaces at temperatures 2 - 6 kK in reactions of reduction of natural silica's with carbon [7]. We investigated experimentally physicochemical processes induced by laser plume on silica glass laser targets streamlined by CH_4 - Ar gas flows, composition and microstructure of products of SiO_2 reduction reactions deposited on substrates [8].

EXPERIMENTAL

Experiments were made with laser targets in the form of cylindrical rods of high-purity and technical-grade silica glass of diameters $d \approx 3$ mm. Experimental setup is shown in Fig.1. A diverging beam from a cw electric-discharge CO_2-laser of ~80 W power was directed on the tip of the rods located behind the focus of an NaCl lens (F = 27 cm) to enhance the stability of the configuration of the resultant laser plume. The radiation intensity was varied by altering the distance from the focus to the target. The targets were placed inside a silica tube of 25 cm length and inner diameter of 15 mm and streamlined by gas flow directed along the tube opposite to the laser beam and escaped freely into atmosphere. A neutral gas flow surrounding the laser target was provided with Ar, whereas reducing flow consisted of CH_4 or of a CH_4 - Ar mixture. The gas flow rate at atmospheric pressure did not exceed 1 liter/min. Silica rods and tubes were used as substrates for the deposition of the laser plume products. The chemical composition of the powder layers deposited on the substrates, sintered or compacted into pellets, was measured with a Camebax SX50 x-ray microanalyser. Microstructure of the laser targets and of the deposited materials was investigated with optical and electron microscopes.

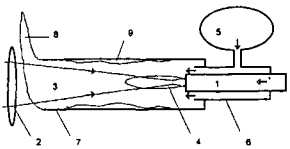

Figure 1. Experimental setup: (1) laser target, (2) NaCl lens, (3) laser beam, (4) laser plume, (5) CH_4 - Ar gaseous mixture, (6) support of the laser target , (7) silica glass tube substrate, (8) flame at the edge of the silica tube, (9) products of the reactions.

RESULTS

At a fixed laser radiation intensity the length of the plume and the spectrum of the emitted radiation depended on the target material. The luminous part of the plume was of ~5 mm length and the emission spectrum was continuous in the visible range when the plume was formed on the surface of high-purity silica glass in an air atmosphere and in Ar. Emission spectra of the plume formed on technical-grade silica glasses included resonance lines of Na and/or K, and the length of the plume increased to ~10 mm. The partly melted and solidified tips of high purity silica glass rods subjected to laser irradiation in atmosphere and Ar had an optically smooth convex shape when the diameter of the laser spot on the end was $d_l > 1/3d$ and a concave shape when d_l was less. Approaching to the focus resulted in a crater formation of ~1 cm deep. The stability of the configuration of targets subjected to laser irradiation was evidently governed by high viscosity of silica glass even at temperature ~T_b.

Radically different results were obtained at the same irradiation geometry when the gas flow around the laser target contained methane. When the gaseous mixture was enriched with methane ([CH_4] > [Ar]) irradiation of the tip of rod target resulted in self-ignition of the flowing gas at the exit from the tube at a distance of 20 cm from the target in the region of contact with atmospheric air. Throughout the whole experiment a spontaneous flame was maintained at the tube exit. Ignition of the laser plume inside the tube resulted in additional coloring of the flame at the tube exit, which became yellow or reddish-orange.

Initially stable at fixed radiation intensity convex shape of the target tip changed with time in the presence of CH_4 - Ar flow by the same manner as by approaching of the target to the focus, i.e. by increasing the intensity. The surface of the target tip became concave and after tens of seconds a conical crater with a diameter of ~1.5 mm and up to several millimeters depth was formed (Fig. 2a). An analysis of the microstructure of the side surface of a laser target showed that interaction of SiO_2 with CH_4 depended on the distance z from the target tip in accordance with the temperature gradient. There were no changes in the surface structure in the zone with a relatively low temperature ($z > 2$ cm) as after annealing in the flame of a methane burner. Uncolored surface husky islands were observed at higher temperatures ($1 < z < 2$ cm). In the zone with a higher temperature ($0.1 < z < 1$ cm) the side surface of a rod became covered by a specular reflecting black film. In the zone with the highest temperature the surface relief at the tip changed more than during irradiation in air. The tip of a target around the region with removed matter was covered by a black glassy film of 50 - 100 μm thickness frothed in the high-temperature zone (Fig. 2b) and smooth in the zone where the temperature was lower at the laser spot periphery. Chip of the film revealed nozzle-like channels of the same characteristic size oriented normally to the surface. The smooth region had fine-grained structure.

The frothed film was displaced on the surface of a glass which was completely covered from the inner side by transparent bubbles of 10 - 20 μm in diameter (Fig. 2c). On the surface of a target irradiated in the high-temperature zone there were hollow spheres with a diameter up to ~100 μm. The spheres were either transparent or outside coated by a white deposited 'soot' and were easily detached (Figs 2d and 2e). Fig. 2f shows bubbles located on the target surface with characteristic traces of a blowout caused by the escape of internal gases. In the low-temperature zone of the glass at a depth up to ~200 μm there were also layers saturated with bubbles with typical size of ~25 μm. Such regions inside some samples contained also whity-brown formations. After irradiation the bottom of a crater remained transparent, i.e. the products of pyrolysis of SiO_2 were removed from the bottom. Instability of the laser target surface resulting on dependence of the rate of etching of SiO_2 at its boundary on the laser radiation intensity was accompanied by shortening of a plume, its subsequent decay, and a reduction of the rate of target 'combustion'.

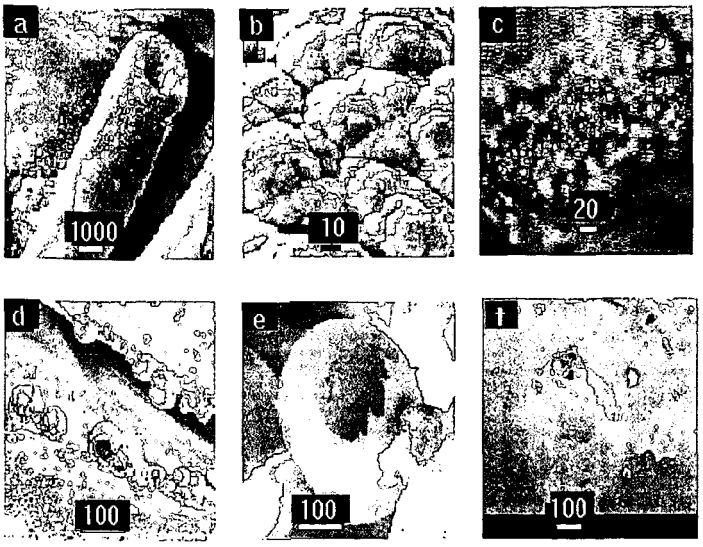

Figure 2. Electron micrographs of laser target (a), boiled and frothed tip of the target (b), bubbles inside (c - photograph) and on surfaces of the targets (d-f).

Vertical convective jet of white smoke emerged from a silica target when the radiation intensity was below the threshold of appearance of a laser plume in an air, $T < T_b$. If the flow of the gas containing CH_4 was repeatedly switched on and off at a constant radiation intensity, a colored plume up to 5 mm length appeared and disappeared in a direction normal to the target tip. This observation indicated that gas-phase reactions took place between the interacting products of a pyrolysis of SiO_2 and CH_4 . Pyrolysis of CH_4 in flowing gaseous mixture interacted with a heated silica rod was indicated by the ejection from the tube of black soot flakes of size up to ~1 cm in accordance with the reaction $CH_4 \rightarrow C + H_2$ at a temperature higher of 800 K. The flakes were formed by a network of filaments of ~0.1 mm in diameter and a very thin layer of a veil-like net between them. These soot flakes emitted bright radiation inside the tube when they crossed the laser beam. It was difficult to carry out x-ray microanalysis because the electron beam destroyed the filaments. There was no self-ignition of the gas by the laser plume when the partial pressure was in the range $1 > [CH_4]/[Ar] > 1/32$ but a self-supporting flame at the tube exit was ignited externally independently on switching the laser plume both on and off. The number of the soot flakes decreased with reducing of CH_4 concentration until they disappeared completely.

Deposition of carried by the flowing gas condensed products on the internal wall of the tube usually lasted the same time as the duration of irradiation of the target (~1 min). The deposited layers were cooled and isolated from the atmosphere by continuing the gas flow for ~30 s after the irradiation. The elemental composition of the deposited materials depended on the partial pressure of methane in the gas flow and deposition place. In particular, the strongly heated surface of the target itself around the laser spot appeared to be a substrate.

A glass-like black film deposited on the target had the chemical composition of a ternary carbosilicate system with depended on temperature concentrations of the components. There were measured ratios of components [Si] : [O] : [C] = 19 : 38 : 42 and 25 : 59 : 16 in two points on the external surface adjoining the tip. On a smooth area of the tip surface around the laser spot ratios [Si] : [O] : [C] = 18 : 21: 60 and 20 : 28 : 52 changed in the direction of a reduction of oxygen and an increase of carbon. This dependence of the composition on the coordinates and, consequently, on the target temperature indicated the reduction reactions occurred on the target.

Black and black-gray layers, mixtures of black and white soot with submicron range microstructure, were deposited on the tube wall when $[CH_4]/[Ar] > 1/16$. The layer thickness reached ~1 mm and the layer density depended on the actual structure of the flowing gas jets determined by the direction of a plume varied during burning of the target and by the local temperature. When the ratio of concentrations in the similar gas flow around a silica target was $[CH]/[Ar] < 1/16$ the ejection of matter from the laser target and the rate of deposition decreased

considerably. The color of the coatings on the tube wall changed being at a distance of 0 - 3 cm from the target tip whity-brown and yellow and at 3 - 15 cm gray. The elemental composition determined at seven points of a pellet compacted from a yellow-brown layer varied within the range [Si] : [O] : [C] = (33:1 - 36:8) : (46:6 - 55:6) : (9:6 - 18.3). The chemical composition of this layer differed considerably from the stoichiometry of the original silica and was the result of the reduction reactions.

DISCUSSION

The chemical composition of final and intermediate products of induced by laser plume chemical reactions was governed by the chemogasdynamic processes on the laser target and between the gas jets containing the products of pyrolysis of methane and silica. Throughout the investigated range of the concentrations $[CH_4]/[Ar]$ used in experiments flammable gases presented in the flow and chemically reducing conditions were maintained. The observed shape of the laser target surface was qualitatively different from that one in oxidizing or neutral ambient gas. It was attributed by narrowing of the thermal energy flux entering target because of additional heating caused by exothermic surface reactions at the maximum intensity in the laser spot. Laser induced chemical reactions occurred not only in gas phase and on the surface but also in the interior of a target, as indicated by laser-induced surface boiling. The appearance of bubbles inside softened silica was attributed by internal gassing occurred when a target was placed in methane flow. Such gas evolution did not occur when plume combustion was maintained in air and Ar. In a control experiment we introduced inside a silica tube of ~2 mm in diameter a bundle of carbon fibers of 10 μm in diameter. Irradiation of the target smelted the fibers with the glass. The glass-fiber boundary was saturated with bubbles and in some cases surrounded by a whity-brown strips.

Boiling of a pure liquid is known to occur because of the appearance of vapor-formation centers, from which bubbles arise inside the liquid, or in a state overheated above the boiling point [9]. The bubbles arise in a liquid if internal pressure $p_i \geq p_a + 2\sigma/r$, where p_a is the atmospheric pressure, σ is the surface tension of silica, r is the bubble radius. In the case under discussion, the quantities σ and r represent the values at the vitrification temperature T_g of silica glass at which the bubble shape becomes frozen. Formation of bubbles from dissolved gases or violent volumetric boiling because of overheating of the liquid phase was not observed in laser targets made of pure silica glass irradiated in atmosphere. Consequently, on the targets streamlined by CH_4 the gas inside the growing bubbles could not consist of the products of pyrolysis of SiO_2 solely becausc p_i could exceed p_a only at temperatures $T > T_b$. The bubbles appeared at lower temperatures and the boundary of the bubble ensemble was mobile at temperatures $T_g \leq T < T_b$.

The most probable reason of observed phenomenon was gas evolution during exothermic chemical reactions in which silica is reduced by carbon and hydrogen occurred inside softened at high temperatures glass. Carbon and hydrogen were appeared on the surface of the rod by pyrolysis of methane and penetrated in the glass by viscous mixing of the melt and diffusion, as indicated by the characteristic shape of whity-brown strips in molten and solidified glass near carbon fibers. Reduction of SiO_2 by carbon $SiO_2 + C \rightarrow Si + SiO + CO$ is used in electrometallurgy for the synthesis of the Si [10]. Silica may be also reduced in the reaction $SiO_2 + H_2 \rightarrow Si + SiO + OH + H_2O$. At temperatures $\sim T_b$ all products of reactions are gaseous because they have lower boiling points. The reactions may cause additional heating of the internal microvolumes of the glass to $T > T_b$ and appearance and growing of microcavities from the gas-formation nuclei filled with gaseous products of the reactions at $p_i > p_a$. A typical shape of the surface at the points of blowout of the bubbles confirmed this hypothesis (Fig.2d). During cooling of the glass the size of the bubbles should decrease and to be frozen at the temperature T_g . This was confirmed by the appearance on a cooled targets of bubbles with concavc dents.

The reduction reactions on the surface of a laser target were initiated at temperatures above the temperature of pyrolysis of methane, ~1 kK, and the rate of these reactions increased with increase in temperature up to the boiling point of silica T_b ~3 kK when a continuous laser plume was formed. The exothermic nature of the reactions was confirmed by lowering of the threshold of formation of a laser plume, when the gas flow contained methane, and supported by increasing of target 'combustion' rate at the maximum intensity in the laser spot as well as by the formation of a crater. The reduction reactions were confirmed also by elemental composition of the laser target surfaces and of the layers of deposited highly disperse products of reactions of whity-brown color. Ratio [Si] : [O] = (79.5 - 46) : (20.5 - 54) on the internal surfaces of four split bubbles indicated that the sample became enriched with silicon being higher of its proportion in silicon monoxide SiO. The reduction processes were observed in experiments with carbon fibers so as droplets of deep-brown color inside the bubbles and evidently formed from more refractory Si and/or SiO.

Deposition of particles on the internal wall of a tube from a high-temperature heterogeneous gas flow occurred under the action of thermophoresys forces similar to the MCVD method employed in the fabrication of silica fiber preforms. Droplets observed inside the bubbles, strips on the boundary of carbon fibers and deposited on substrates powder layers all of yellow, whity- and deep-brown colors are the products of the disproportion reaction of reduced but unstable condensed silicon oxide $SiO \rightarrow Si + SiO_2$. It was last time determined that gradation of color is connected with microstructure of the samples containing amorphous and microcrystalline silicon.

CONCLUSION

Experimentally were established the experimental conditions, the configuration, and the energy and gasdynamic parameters of initiation by cw laser radiation at the 10.6 mm wavelength of chemical reduction of silica streamlined by gas flow containing methane. The exothermic nature of the reduction reactions was confirmed by decrease of the threshold of appearance of a laser plume and increase in the rate of combustion of the target in the laser spot and formation of a crater so as by an increase in the yield of the reaction products deposited on the tube wall, compared with the yield of the products of pyrolysis of silica in air, and also by a fall of the yield when the concentration of methane in the flowing gas was lowered.
The determined final products of laser-induced reactions of silica with methane are conductive carbosilicate films on silica surfaces and reduced silicon oxides in gas and condensed phases.

REFERENCES

1. Dianov E M, Koryakovsky A S, Lebedev V F, Marchenko V M, Prokhorov A M Zh. Tekh. Fiz. 61 (5) 90 (1991) [Sov. Phys. Tech. Phys. 36 551 (1991)]; Sov. Lightwave Commun. 1 223 (1991)
2. Shick H. L. Chem. Rev. 60 331 (1960)
3. Kulikov I. S. Termicheskaya Dissotsiatsiya Soedinenij (Thermal Dissociation of Compounds) (Moscow: Metallurgiya, 1969)
4. Dianov E. M., Lavrishchev S. V., Marchenko V. M., Mashinsky V. M., Prokhorov A. M. Kvantovaya Elektron. (Moscow) 23 1105 (1996) [Quantum Electron. 26 1075 (1996)]
5. Dianov E.M., Koryakovsky A. S., Marchenko V. M., Lebedev V. F., Pimenov V. G., Prokhorov A M Zh. Tekh. Fiz. 63 (11) 196 (1993) [Tech. Phys. 38 1030 (1993)]
6. Sosman R. B. Phases of Silica (New Brunswick, NJ: Rutgers University Press, 1965)
7. Wolf S., Tauber R. N. Silicon Processing for the VLSI Era (Sunset Beach, CA: Lattice Press, 1996)
8. Lavrishchev S.V., Marchenko V.M., Murin D.I. Quantum Electronics, 28, 920 (1998)
9. Kikoin A. K., Kikoin I. K. Molekulyarnaya Fizika (Molecular Physics) (Moscow: Nauka, 1978)
10. Gel'd P. V., Esin O. A. Protsessy Vysokotemperaturnogo Sinteza (Processes in High-Temperature Synthesis) (Sverdlovsk: State Scientific-Research Institute on Ferrous and Nonferrous Metallurgy, 1957)